ARTICLE IN PRESS
JID: JMAA [m5+;June 27, 2023;3:52]

Available online at www.sciencedirect.com

ScienceDirect

Journal of Magnesium and Alloys xxx (xxxx) xxx

www.elsevier.com/locate/jma

A combined experimental and crystal plasticity study of grain size effects in magnesium alloys

Aaditya Lakshmanan[a], Mohsen Taheri Andani[b,c], Mohammadreza Yaghoobi[b,*], John Allison[b], Amit Misra[b,c], Veera Sundararaghavan[a]

[a] Department of Aerospace Engineering, University of Michigan, Ann Arbor, MI, 48105, USA
[b] Department of Materials Science and Engineering, University of Michigan, Ann Arbor, MI, 48105, USA
[c] Department of Mechanical Engineering, University of Michigan, Ann Arbor, MI, 48105, USA

Received 7 October 2022; received in revised form 27 March 2023; accepted 22 May 2023
Available online xxx

Abstract

This work presents a method to incorporate the micro Hall-Petch equation into the crystal plasticity finite element (CPFE) framework accounting for the microstructural features to understand the coupling between grain size, texture, and loading direction in magnesium alloys. The effect of grain size and texture is accounted for by modifying the slip resistances of individual basal and prismatic systems based on the micro Hall-Petch equation. The modification based on the micro Hall-Petch equation endows every slip system at each microstructural point with a slip system-level grain size and maximum compatibility factor, which are in turn used to modify the slip resistance. While the slip-system level grain size is a measure of the grain size, the maximum compatibility factor encodes the effect of the grain boundary on the slip system resistance modification and is computed based on the Luster-Morris factor. The model is calibrated using experimental stress-strain curves of Mg-4Al samples with three different grain sizes from which the Hall-Petch coefficients are extracted and compared with Hall-Petch coefficients predicted using original parameters from previous work. The predictability of the model is then evaluated for a Mg-4Al sample with different texture and three grain sizes subjected to loading in different directions. The calibrated parameters are then used for some parametric studies to investigate the variation of Hall-Petch slope for different degrees of simulated spread in basal texture, variation of Hall-Petch slope with loading direction relative to basal poles for a microstructure with strong basal texture, and variation of yield strength with change in grain morphology. The proposed approach to incorporate the micro Hall-Petch equation into the CPFE framework provides a foundation to quantitatively model more complicated scenarios of coupling between grain size, texture and loading direction in the plasticity of Mg alloys.

Keywords: Hall-Petch; Crystal plasticity; Grain size; Texture; Magnesium alloys.

1. Introduction

The low density of Mg alloys allows for significant weight reduction in product development, making them strong candidates for applications in the aerospace [1], automotive [2] and medical [3] sectors. However, one of the major drawbacks in their widespread use is their poor formability and ductility at room temperature that arises from the hexagonal close-packed crystal structure ($c/a = 1.624$). Unlike Al alloys with a cubic crystal structure which possess twelve equivalent slip systems to accommodate plastic deformation, Mg alloys depict significant plastic anisotropy where prismatic and pyramidal systems have significantly higher critical resolved shear stress (CRSS) relative to the three basal slip systems. Due to this limitation, efforts have focused on tailoring the microstructure to enhance the ductility of Mg alloys. Strategies that attempt to achieve this include, but are not limited to, precipitation hardening [4–7], solid-solution strengthening [8–10], texture control [11,12] and grain refinement [13,14].

* Corresponding author.
E-mail address: yaghoobi@umich.edu (M. Yaghoobi).

https://doi.org/10.1016/j.jma.2023.05.008

The study of the effect of grain refinement on the yield strength dates back to the classical work by Hall [15] and Petch [16], where a linear relationship was drawn between the lower yield point of mild steel (σ_Y) and the inverse square-root of the average grain size (d), loosely based on the Eshelby-Frank-Nabarro solution [17] to a discrete dislocation pile-up model:

$$\sigma_Y = \sigma_0 + \frac{K_{HP}}{\sqrt{d}} \quad (1)$$

where σ_0 is the intercept (Hall-Petch intercept) of the linear relationship and denotes the grain size-independent component of the yield strength, and K_{HP} is the slope of the linear relation. K_{HP} is referred to as the "locking parameter" or Hall-Petch slope; we use the latter in the paper. Similar empirical power-law relationships have also been found for other mechanical properties of polycrystalline materials in alloys other than mild steel [18], which motivated a myriad of similar studies for various Mg alloys [13,19-25]. Cordero et al. [26] have presented an extensive review of the Hall-Petch effect while Yu et al. [14] have reviewed previous work on Hall-Petch relationship with specific focus on Mg alloys.

A characteristic of Mg alloys is the strong dependence of the Hall-Petch slope on the crystallographic texture, as evidenced by previous experimental studies [13,20,24,27]. For example, Wang et al. [24] studied the tensile behavior of a commercial Mg AZ31B alloy exhibiting basal texture, relative to four average grain sizes and five different loading directions. They reported values of σ_0 in the range 12 - 42 MPa and the Hall-Petch slope K_{HP} in the range 158 - 411 MPa $\mu m^{0.5}$. In another study, Wang et al. [20] studied the tensile deformation of friction stir processed and extruded Mg AZ31B alloy specimens with a set of different grain sizes along the advancing direction. They observed a strong texture dependence of the yield strength on the grain size for extruded samples recording $\sigma_0 \approx$ 80MPa and $K_{HP} \approx$ 303 MPa $\mu m^{0.5}$. This was in contrast to relatively weaker texture dependence for friction stir processed samples with $\sigma_0 \approx$ 10MPa and $K_{HP} \approx$ 160 MPa $\mu m^{0.5}$ [20]. Guan et al. [12] proposed a simple equation based on a dislocation pile-up model to compute K_{HP} for Mg AZ31B alloy for different textures depending on two effective parameters, which are based on the expected active slip systems.

Simulations based on crystal plasticity constitutive models have proven to be a powerful tool to derive insights into the mechanical behavior of polycrystalline microstructures by integrating the single-crystal constitutive models with the governing equations of continuum mechanics. While classical crystal plasticity constitutive models have been extremely useful [28–33], by construction they are unable to capture the difference in mechanical behavior that arises from changes in the internal microstructural length scale, like the grain size. To address this issue, one alternative has been the strain-gradient plasticity approach, which has proven particularly useful in capturing the intrinsic size effects arising in several plasticity-related phenomena [34–38]. However, these models are relatively expensive to evaluate and also pose a challenge for parameter calibration since they involve a large number of internal variables. Additionally, the microscopic variables derived from the strain gradients are used to inform the hardening behavior while the effect of the microstructural length scale on the initial CRSS is set phenomenologically. A simpler alternative has been to include a grain size-dependent contribution to the CRSS of individual slip systems by simply extending the Hall-Petch relationship to individual slip systems (see, e.g., Lakshmanan et al. [39]). Based on such a modification, there have been very few computational studies addressing the coupling between grain size and texture in Mg alloys. Jain and coworkers [40,41] have conducted studies using a grain size-dependent viscoplastic self-consistent crystal plasticity (VPSC) model on a rolled Mg alloy to investigate the role of grain size associated with prismatic slip during the tensile experiment. Raesinia et al. [42] fit the affine VPSC model to the data in Jain et al. [41] through uniform scaling of the CRSS to establish a slip system-level Hall-Petch relationship, which involves the slip system-level Hall-Petch coefficient and the average grain size. Such VPSC models have also been used to explore the role of grain size on the twin growth [43], the density of twins [44], and also the correlation between the crystallographic orientation of the grain and the corresponding twin variant selected [45]. Ganesan et al. [46] calculated the slip system-level Hall-Petch coefficient for different slip systems in WE43 Mg alloy using CPFE simulation. Ravaji et al. [47] investigated the interacting effects between the grain size, loading direction and texture on the response of an Mg alloy. They investigated the role of grain size-texture coupling in reducing the net plastic anisotropy, the tension-compression asymmetry and the tempering of extension twinning with grain refinement across different textures and loading directions. Common in all these important studies is that a single average grain size is used to modify the CRSS for all the grains in the simulated microstructure. Moreover, this modification to the CRSS at the slip system level, which resembles the linear dependence on the inverse square-root of the average grain size, uses a constant Hall-Petch type parameter for a particular slip system for all the grains in the microstructure. In other words, the microstructural features are not captured directly in the parts of the constitutive model accounting for the grain size effect.

Such an inclusion of the microstructural features builds on our recent work [48–50] which uses the micro Hall-Petch equation as the basis for including the grain size effect in our constitutive model:

$$\tau^\alpha = \tau_0^\alpha + \tau_g^\alpha = \tau_0^\alpha + \frac{k_\mu^\alpha}{\sqrt{d^\alpha}} \quad (2)$$

where τ^α denotes the initial slip resistance (identical to CRSS) associated with slip system α, decomposed into a grain size-independent contribution (τ_0^α) and grain size-dependent contribution (τ_g^α). Additionally, this grain size-dependent contribution has a form similar to the classical Hall-Petch equation but extended to the slip system level where k_μ^α denotes the micro Hall-Petch parameter and d^α is a measure of the slip system-level grain size. Taheri Andani et al. [49,50] inte-

Please cite this article as: A. Lakshmanan, M.T. Andani, M. Yaghoobi et al., A combined experimental and crystal plasticity study of grain size effects in magnesium alloys, Journal of Magnesium and Alloys, https://doi.org/10.1016/j.jma.2023.05.008

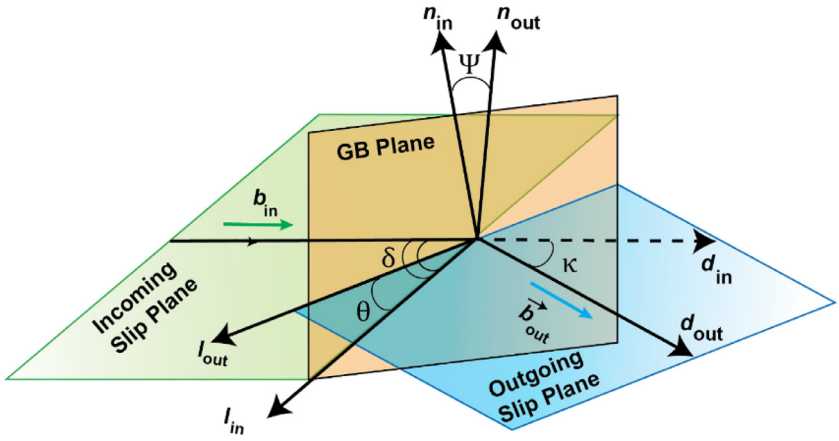

Fig. 1. A schematic representative for slip transmission through a GB. $\vec{b}_{in}$: Burgers vector of the incoming slip system, $\vec{b}_{out}$: Burgers vector of the outgoing slip system, $\vec{n}_{in}$: Slip plane normal of the incoming slip system, $\vec{n}_{out}$: Slip plane normal of the outgoing slip system, $\vec{l}_{in}$: Intersection line of the incoming slip plane and GB, $\vec{l}_{out}$: Intersection line of the outgoing slip plane and GB, $\vec{d}_{in}$: Slip direction of the incoming slip system, $\vec{d}_{out}$: Slip direction of the outgoing slip system, θ: Angle between the two slip plane traces on the grain boundary plane, κ: Angle between slip directions, ψ: Angle between slip plane normal, δ: Angle between the incoming slip direction and the incoming slip plane trace on the grain boundary plane.

grated experimental measurements of pile-up stress ahead of slip bands blocked by a grain boundary, with a dislocation pile-up model and crystal plasticity simulations, to obtain an empirical power-law relationship between k_{μ}^{α} and certain geometrical descriptors of the grain boundaries for basal and prismatic slip systems:

$$k_{\mu}^{\alpha} = K_{\mu}^{\alpha}\,[1-\cos\,(\theta)\cos\,(\kappa)]^{c^{\alpha}} \tag{3}$$

where K_{μ}^{α} is the micro Hall-Petch multiplier and c^{α} is the micro Hall-Petch exponent, respectively, for the slip system α. θ and κ denote angular quantities obtained from knowledge of the slip systems in neighboring grains and the grain boundary inclination, respectively (Fig. 1). As a result of these studies, K_{μ}^{α} and c^{α} were estimated for basal [49] and prismatic [50] slip systems, providing quantitative insights into the role of grain boundaries in informing the grain size-dependent contribution to the slip resistance. Additionally, in the interest of implementing such a relationship in crystal plasticity constitutive models, a similar power-law relationship was drawn where instead of the angle θ, the angle ψ, was used:

$$k_{\mu}^{\alpha} = K_{\mu}^{\alpha}\,[1-\cos\,(\psi)\cos\,(\kappa)]^{c^{\alpha}} \tag{4}$$

where the factor $\cos(\psi)\cos(\kappa)$ is also commonly referred to as the Luster-Morris factor [51,52]. This aspect is particularly important in the context of computational representation of microstructures since grain boundary inclination in synthetic microstructures is sensitive to the mesh used in their discretization. The relationship in Eq. (4) provides a way to sidestep the grain boundary information, and as a first attempt only includes the relative crystallographic orientation between grains as the key factor in parametrizing the micro Hall-Petch parameter.

In this work, we present our attempts to implement the micro Hall-Petch equation into a crystal plasticity simulation framework. We first briefly outline the rate-dependent crystal plasticity constitutive model implemented into the open-source PRISMS-Plasticity crystal plasticity finite element (CPFE) framework [53–57], that is used for all our simulations. Then, we outline the procedure to compute the micro Hall-Petch parameter, k_{μ}^{α}, and the slip system-level grain size, d^{α}, which forms part of the preprocessing step to then modify the slip resistances based on the micro Hall-Petch equation. Subsequently, the model is calibrated with experimental stress-strain curves of Mg-4Al samples from which the Hall-Petch parameters are extracted, followed by a comparison with predictions from original parameters reported in previous work [49,50]. The calibrated set of parameters are then used to perform three parametric studies: (i) Study the variation of the Hall-Petch slope for different degrees of simulated spread of basal texture, (ii) Study the variation of the Hall-Petch slope for different angles of loading direction relative to basal poles for a microstructure with strong basal texture, and (iii) Study the variation of the yield strength relative to changes in the morphology of the grains in the microstructure.

2. Computational and experimental methods

2.1. Crystal plasticity model

A rate-dependent crystal plasticity constitutive model is adopted within the framework of finite deformation continuum mechanics. The primary kinematic quantity is the deformation gradient, $\mathbf{F}$, which maps tangent vectors in the reference configuration to corresponding vectors in the deformed configuration. Assuming $\mathbf{F}$ abides by a multiplicative decomposition [58,59] into elastic ($\mathbf{F}^{e}$) and plastic ($\mathbf{F}^{p}$) components as follows:

$$\mathbf{F} = \mathbf{F}^{e}\mathbf{F}^{p} \tag{5}$$

$\mathbf{F}^{p}$ encodes the distortion of the body as a result of crystallographic slip via dislocation motion on specific slip systems and maps the reference configuration to an intermediate configuration where the underlying lattice remains unchanged.

Please cite this article as: A. Lakshmanan, M.T. Andani, M. Yaghoobi et al., A combined experimental and crystal plasticity study of grain size effects in magnesium alloys, Journal of Magnesium and Alloys, https://doi.org/10.1016/j.jma.2023.05.008

$\mathbf{F}^{\mathrm{e}}$ captures the elastic stretch and lattice rotation and maps the intermediate configuration to the deformed configuration. Since plasticity is inherently deformation path-dependent we invoke certain deformation rates to further develop the constitutive model. Using Eq. (5), the velocity gradient, $\mathbf{L} = \dot{\mathbf{F}}\mathbf{F}^{-1}$, can be decomposed into elastic and plastic components:

$$L = \underbrace{\dot{F}^e F^{e-1}}_{Elastic part} + \underbrace{F^e \dot{F}^p F^{p-1} F^{e-1}}_{Plastic part} \tag{6}$$

Contributions to the velocity gradient from elastic and plastic parts are both defined in the deformed configuration. We can alternatively work with the plastic part of the velocity gradient defined on the intermediate configuration, $\mathbf{L}^{\mathrm{p}}$, as:

$$\mathbf{L}^{\mathrm{p}} = \dot{\mathbf{F}}^{\mathrm{p}}\mathbf{F}^{p-1} \tag{7}$$

Noting that the kinematics of crystallographic slip effectively involves shearing of the lattice on specific crystallographic slip planes along with specific crystallographic slip directions, we have

$$\mathbf{L}^{\mathrm{p}} = \dot{\mathbf{F}}^{\mathrm{p}}\mathbf{F}^{p-1} = \sum_{\alpha=1}^{n_s+n_t} \dot{\gamma}^{\alpha}\mathbf{m}^{\alpha} \otimes \mathbf{n}^{\alpha} = \sum_{\alpha=1}^{n_s+n_t} \dot{\gamma}^{\alpha}\mathbf{S}^{\alpha} \tag{8}$$

where $\dot{\gamma}^{\alpha}$ is the shearing rate on slip system α, n_s is the number of slip systems, n_t is the number of twin systems, $\mathbf{m}^{\alpha}$ and $\mathbf{n}^{\alpha}$ are slip direction and slip plane normal unit vectors, respectively. $\mathbf{S}^{\alpha}$, referred to as the Schmid tensor for the slip/twin system α, is a shorthand for the dyadic product of $\mathbf{m}^{\alpha}$ and $\mathbf{n}^{\alpha}$. We note that $\mathbf{m}^{\alpha}$ and $\mathbf{n}^{\alpha}$ are crystallographic vectors in the intermediate configuration.

We adopt a rate-dependent crystal plasticity framework, where the shearing rate $\dot{\gamma}^{\alpha}$ is a function of the resolved shear stress τ^{α} through a phenomenological power law as follows [60]:

$$\dot{\gamma}^{\alpha} = \dot{\gamma}_0 \left| \frac{\tau^{\alpha}}{s^{\alpha}} \right|^{m} \mathrm{sign}(\tau^{\alpha}) \tag{9}$$

where $\dot{\gamma}_0$ is the reference shearing rate, m is the strain rate sensitivity exponent, τ^{α} is the resolved shear stress on slip/twin system α, s^{α} is the slip resistance on slip/twin system α and 'sign' refers to the signum function. The resolved shear stress is expressed in terms of the second Piola-Kirchoff stress in the intermediate configuration [61,62], $\mathbf{T}$, via the following relation

$$\tau^{\alpha} = \left(\mathbf{F}^{\mathrm{eT}}\mathbf{F}^{\mathrm{e}}\mathbf{T}\right) : \mathbf{S}^{\alpha} \tag{10}$$

where ': ' denotes the inner product of second order tensors defined as $\mathbf{A}$: $\mathbf{B} = A_{ij}B_{ij}$. Eq. (10) is derivable by equating the plastic part of the internal mechanical power to the power expended in crystallographic shearing of slip/twin system α with resolved shear stress τ^{α} and shearing rate $\dot{\gamma}^{\alpha}$. The second Piola-Kirchoff stress in the intermediate configuration is linked to the elastic Green-Lagrange strain as follows:

$$\mathbf{T} = \mathcal{L} \cdot \mathbf{E}^{\mathrm{e}} = \frac{1}{2}\mathcal{L} \cdot \left(\mathbf{F}^{\mathrm{eT}}\mathbf{F}^{\mathrm{e}} - \mathbf{I}\right) \tag{11}$$

where $\mathbf{E}^{\mathrm{e}}$ is the elastic Green-Lagrange strain tensor, $\mathcal{L}$ is the elastic stiffness tensor (a fourth-order tensor) and $\mathbf{I}$ is the second-order identity tensor. ' $\cdot$ ' denotes the product between a fourth-order tensor and second-order tensor to furnish a resultant second-order tensor, defined as $(\mathcal{L} \cdot \mathbf{A})_{ij} = \mathcal{L}_{ijkl}A_{kl}$. We additionally note that the Cauchy stress, $\boldsymbol{\sigma}$, and the first Piola-Kirchoff stress in the reference configuration, $\mathbf{P}$, are related to $\mathbf{T}$ as follows:

$$\mathbf{T} = \mathbf{F}^{e-1}\mathbf{P}\ \mathbf{F}^{T}\mathbf{F}^{e-T} = \det\ (\mathbf{F}^{\mathrm{e}})\mathbf{F}^{e-1}\boldsymbol{\sigma}\ \mathbf{F}^{e-T} \tag{12}$$

Finally, the evolution of slip resistance for slip system α, which governs isotropic hardening, is defined as follows [62]:

$$\dot{s}^{\alpha} = \sum_{\beta=1} h^{\alpha\beta}\dot{\gamma}^{\beta} \tag{13}$$

where $h^{\alpha\beta}$ denotes the hardening rate on slip/twin system α due to the slip on system β. The initial slip resistance for each slip/twin system is defined as follows:

$$s^{\alpha}\ (0) = s_0^{\alpha} + s_g^{\alpha} = s_0^{\alpha} + \frac{k_{\mu}^{\alpha}}{\sqrt{d^{\alpha}}} \tag{14}$$

where s_0^{α} and s_g^{α} denote the size-independent and size-dependent contributions, respectively, to the initial slip resistance. s_g^{α} is assumed to hold a functional-form identical to the classical Hall-Petch equation, but now extended to the level of an individual slip system, with k_{μ}^{α}denoting the micro Hall-Petch multiplier and d^{α} denoting a measure of the slip system-level grain size. The hardening moduli $h^{\alpha\beta}$ are prescribed via a power-law relationship involving the combined effect of work hardening and recovery, with both self and latent hardening contributions as follows:

$$h^{\alpha\beta} = \begin{cases} h_0^{\beta}\left[1 - \frac{s^{\beta}}{s_s^{\beta}}\right]^{a^{\beta}}; & \text{coplanar systems} \\ h_0^{\beta} q\left[1 - \frac{s^{\beta}}{s_s^{\beta}}\right]^{a^{\beta}}; & \text{otherwise} \end{cases} \tag{15}$$

Where h_0^{β} denotes the hardening parameter for slip/twin system β, q is the latent hardening ratio, s_s^{β} is the saturation slip resistance for slip/twin system β, and a^{β} is a material constant for slip/twin system β governing the sensitivity of the hardening moduli to the slip resistance.

The final aspect of the model is to capture reorientation due to twinning. In the current framework, the PTR scheme developed by Tomé et al. [63] is incorporated to capture twinning. The twinning is modeled as pseudo-slip system, and the nominal twin volume fraction for k^{th} twin system, i.e., f_{tw}^{k*}, can be evolved as follows:

$$\dot{f}_{tw}^{k*} = \frac{\dot{\gamma}^{k}}{S} \tag{16}$$

where S is the characteristic twin shear strain, which is calculated as 0.129 for Mg [53]. According to the PTR scheme, when f_{tw}^{k*} for any twin system becomes larger than a specific threshold of F_T, the grain will be reoriented according to that twin system. The threshold F_T can be defined as follows [53,63]:

$$F_T = A + B\frac{F_E}{F_R} \tag{17}$$

Please cite this article as: A. Lakshmanan, M.T. Andani, M. Yaghoobi et al., A combined experimental and crystal plasticity study of grain size effects in magnesium alloys, Journal of Magnesium and Alloys, https://doi.org/10.1016/j.jma.2023.05.008

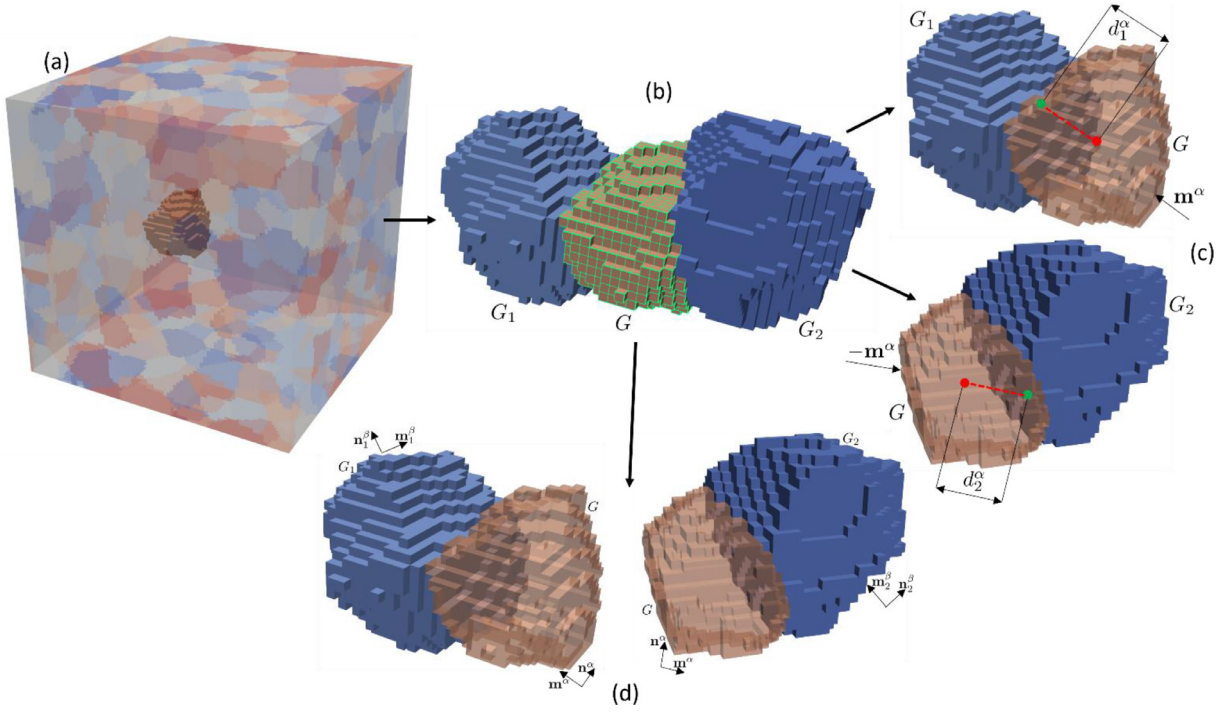

Fig. 2. Illustration depicting the workflow described in Section 2.2 to compute d^α and k_μ^α. (a) Voxelated microstructure from DREAM.3D. (b) For any microstructural point in grain G and line passing through it with slip direction $\mathbf{m}^\alpha$, find the neighboring grains G_1 and G_2 based on the points of intersection of the line with the boundary. (c) The slip system level grain size d^α is computed for every point in the microstructure by finding the length of the line segment passing through that point connecting the two points on the grain boundary with direction $\mathbf{m}^\alpha$. (d) To compute k_μ^α the primary quantity is the maximum compatibility factor which is computed using the knowledge of slip systems corresponding to the neighboring grains G_1 and G_2. The neighboring grains are identified by the neighbors of G that share each of the two points on the grain boundary that were found for computing d^α.

where F_E is the total reoriented twin volume within the sample and F_R is the total nominal twin volume fraction within the sample. The twinning model constants are set to $A = 0.7$ and $B = 0$ similar to the values used in Yaghoobi et al. [53]. The constitutive model is implemented in the PRISMS-Plasticity CPFE code [53,54] an open-source, scalable software framework to simulate elasto-plastic boundary value problems built on top of the deal.II [64] open source finite element (FE) library.

2.2. Micro Hall-Petch constitutive model

The initial slip resistance consists of a size-independent and a size-dependent contribution, with the size dependent contribution dictates by the micro Hall-Petch parameter, k_μ^α, and slip system-level grain size, d^α. The computation of k_μ^α includes information concerning the grain neighbors while d^α encodes the information of both the grain size and grain morphology. We now outline the procedure followed in computing these key quantities, as shown in Fig. 2.

Let's assume we are given a microstructure discretized as a uniform grid of voxels, along with information about the grains, i.e., a set of grain identifiers (integers), and the orientation associated with those identifiers. With this input, d^α is computed for each voxel of the microstructure as follows:

1. Consider any particular voxel defined by its centroidal coordinates $\mathbf{p}_c = (x_c, y_c, z_c)$ along with the corresponding grain, G, it belongs to. With this voxel fixed, consider slip system α for which we wish to compute k^α and d^α. Let $\mathbf{m}^\alpha$ denote the slip direction associated with slip system α.
2. For grain G, identify its boundary ∂G, which is essentially a collection of rectangular faces.
3. Find the point $\mathbf{p}_1$ on ∂G closest[1] to point $\mathbf{p}_c$ along direction $\mathbf{m}^\alpha$ and denote this closest distance by d_1^α.
4. Find the point $\mathbf{p}_2$ on ∂G closest to point $\mathbf{p}_c$ along direction -$\mathbf{m}^\alpha$and denote this closest distance by d_2^α.
5. Define the slip system-level grain size d^α by $d^\alpha = d_1^\alpha + d_2^\alpha$. A very similar methodology has been adopted by Nieto-Valeiras et al. [65], where the computed distances were used in dislocation-density evolution equations to study the effect of slip transfer at GBs on the strength of FCC polycrystals.

In the next step, k_μ^α is computed as follows:

1. Having computed points $\mathbf{p}_1$ and $\mathbf{p}_2$ the neighboring grains sharing these points with grain G are first found. Denote them by G_1 and G_2, respectively.

[1] Since the grain G need not be a convex set.

Please cite this article as: A. Lakshmanan, M.T. Andani, M. Yaghoobi et al., A combined experimental and crystal plasticity study of grain size effects in magnesium alloys, Journal of Magnesium and Alloys, https://doi.org/10.1016/j.jma.2023.05.008

2. Define $\psi_1^{\alpha\beta}$ as the angle satisfying the relation $\cos(\psi_1^{\alpha\beta}) = \mathbf{n}^\alpha \cdot \mathbf{n}_1^\beta$ where $\mathbf{n}^\alpha$ is the slip plane normal corresponding to slip system α and $\mathbf{n}_1^\beta$ is the slip plane normal corresponding to slip system β in G_1. Define $\kappa_1^{\alpha\beta}$ as the angle satisfying the relation $\cos(\kappa_1^{\alpha\beta}) = \mathbf{m}^\alpha \cdot \mathbf{m}_1^\beta$ where $\mathbf{m}^\alpha$ is the slip plane corresponding to slip system α and $\mathbf{m}_1^\beta$ is the slip plane corresponding to slip system β in G_1.
3. Compute the compatibility factor defined as $|\cos(\psi_1^{\alpha\beta})\cos(\kappa_1^{\alpha\beta})|$ ($|\ .\ |$ denotes the absolute value) for all β and identify the maximum over all β. Denote this maximum by μ_1^α.
4. Define $\psi_2^{\alpha\beta}$ as the angle satisfying the relation $\cos(\psi_2^{\alpha\beta}) = \mathbf{n}^\alpha \cdot \mathbf{n}_2^\beta$ where $\mathbf{n}^\alpha$is the slip plane corresponding to slip system α and $\mathbf{n}_2^\beta$ is the slip plane corresponding to slip system β in G_2. Define $\kappa_2^{\alpha\beta}$ as the angle satisfying the relation $\cos(\kappa_2^{\alpha\beta}) = \mathbf{m}^\alpha \cdot \mathbf{m}_2^\beta$ where $\mathbf{m}^\alpha$is the slip plane corresponding to slip system α and $\mathbf{m}_2^\beta$ is the slip plane corresponding to slip system β in G_2.
5. Compute the compatibility factor defined as $|\cos(\psi_2^{\alpha\beta})\cos(\kappa_2^{\alpha\beta})|$ for all β and identify the maximum over all β. Denote this maximum by μ_2^α.
6. Define $\mu^\alpha := \max(\mu_1^\alpha, \mu_2^\alpha)$ and compute k_μ^α using the micro Hall-Petch equation as $k_\mu^\alpha = K_\mu^\alpha(1-\mu^\alpha)^{c^\alpha}$, where K_μ^α is the micro Hall-Petch multiplier, c^α is the micro Hall-Petch exponent fixed for the material under consideration and μ^α is referred to as the maximum compatibility factor, which is computed for every slip system and every microstructural point. Typically, the lower the misorientation is between grains, the higher is the maximum compatibility factor, with the maximum possible value being 1 since it is computed from a multiplication of cosines.

The computation of d^α and k_μ^α outlined above is implemented in an open-source MATLAB script (see **Code Availability** below), which is used as a preprocessor to generate this data in a format readable by PRISMS-Plasticity CPFE.

2.3. Materials and experimental procedures

Extruded Mg-4Al (wt.%) bars provided by CanmetMaterials are used in this work, with the following composition (wt%): Al-3.4, Cu-0.005, Fe-0.006, Mn-0.02, Ni-0.005, Si-0.08, Zn-0.01. As-received extruded samples were used in this study, along with heat treated samples (to increase grain size) and compressed and heat-treated samples (to provide a variation in texture). The texture of the as-received material and the compressed samples (5% compression along the extrusion direction following heat treatment at 300 °C for 3 h) with average grain sizes of 55 μm and 68 μm, respectively, are shown in Fig. 3(a) and Fig. 3(b). The average grain sizes were calculated directly from the OIM images using grain-to-grain measurements. Additional heat treatment was conducted on the as-received samples to provide specimens with average grain sizes of approximately 187 μm (515 °C for 15 min) and 333 μm (550 °C for 150 min) with textures very similar to the starting texture (Texture 1). Similarly, additional heat treatment was conducted on the compressed samples to provide specimens with average grain sizes of approximately 227 μm (515 °C for 15 min) and 343 μm (550 °C for 150 min) with textures very similar to the texture of the compressed sample (Texture 2).

Crystallographic orientation information was obtained using electron backscatter diffraction (EBSD). Scans were conducted using a Tescan Mira 3 scanning electron microscope equipped with an EDAX Hikari XP EBSD detector. Each scan was captured at a voltage of 30 kV and a beam intensity of 20 nA with an average step size of 1 μm. The samples are mechanically ground using SiC papers up to a grit of 1200. Polishing is completed using three steps 6 μm, 3 μm, and 1 μm diamond suspensions, followed by a final polish using Buehler Masterpolish on a Buehler Chemomet polishing cloth. Finally, samples are chemically etched in acetic-nitric solution (60 mL ethanol, 20 mL water, 15 mL acetic acid, and 5 mL nitric acid) for 3–5 s. Tensile tests are conducted on samples with the gauge dimensions of 10 mm × 2 mm × 2 mm using INSTRON load frame equipped with a 100 kN load cell at a constant displacement rate of 1 μm/second. The macroscopic strain was measured using an extensometer attached to the sample. Mechanical testing was performed on three samples per texture-loading pair.

2.4. Preprocessing

2.4.1. Synthetic microstructure generation

The procedure to generate synthetic microstructures for the CPFE simulation using DREAM.3D [66] is presented in this section. The primary inputs required by DREAM.3D to generate microstructures are texture and grain size distribution. For each of the nine cases, the input from microscopy is an EBSD orientation map consisting of the orientations of the pixels in the pixelated image of a 2D section of the microstructure (Fig. 4a). MTEX [67], a free MATLAB toolbox for texture analysis, is used to read in the EBSD map, compute the ODF and pole figures (Fig. 4d), and write out this EBSD data in a format readable by DREAM.3D. For the grain size distribution data, the equivalent grain sizes for all the grains in the 2D section are straightforward to obtain using MTEX. However, this furnishes a 2D measure of grain size, which is always an underestimation of the real grain size because these EBSD maps are 2D sections. The way we addressed this issue is to use the 2D equivalent grain size statistics (Fig. 4b) obtained from MTEX along with the Scheil-Schwartz-Saltykov method [68–70] to obtain the 3D grain size statistics, assuming equiaxed grains. Saltykov [70] proposed a general algorithm to compute the probability distribution of spheres of different sizes, given information about the apparent sizes (from 2D sections). The 3D grain size statistics are then fit with a lognormal distribution (Fig. 4c), whose characteristic parameters (mean and variance) are fed into DREAM.3D to generate synthetic microstructures (Fig. 4e). When comparing the mean 2D grain size with the mean from the lognormal

Please cite this article as: A. Lakshmanan, M.T. Andani, M. Yaghoobi et al., A combined experimental and crystal plasticity study of grain size effects in magnesium alloys, Journal of Magnesium and Alloys, https://doi.org/10.1016/j.jma.2023.05.008

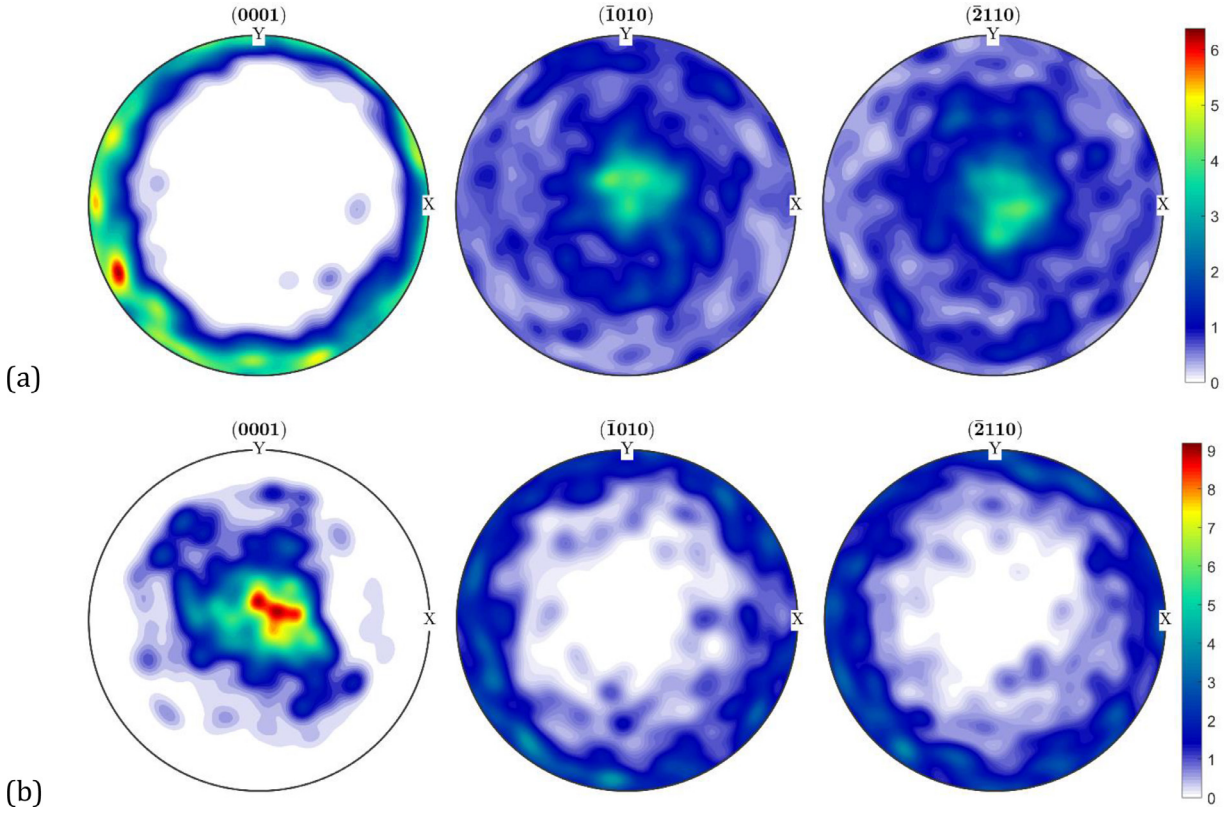

Fig. 3. (a) Texture 1: As-extruded texture for which the specimens with the three average grain sizes are deformed in tension along the extrusion direction (z-direction), (b) Texture 2: Close to basal texture for which the specimens with the three average grain sizes are deformed in two separate ways: (i) tension along the z-direction and (ii) tension along the x-direction.

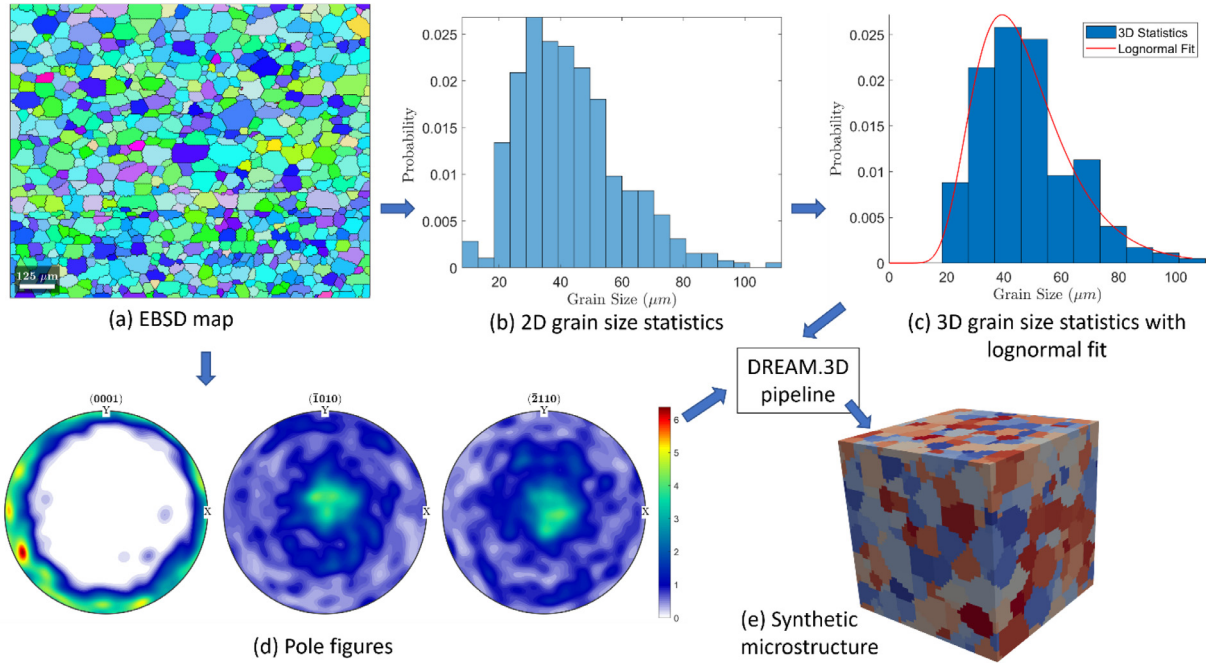

Fig. 4. Illustration depicting the workflow described in Section 2.4.1 to obtain necessary inputs for synthetic microstructure generation in DREAM.3D. (a) 2D microstructure section from experiment, (b) 2D grain size statistics extracted from microstructure section, (c) Use Saltykov's method to obtain 3D grain size statistics and fit it with lognormal distribution, (d) Pole figures from experimental texture data, (e) Use best-fit lognormal distribution parameters and pole figures as input to DREAM.3D to generate synthetic microstructure.

Please cite this article as: A. Lakshmanan, M.T. Andani, M. Yaghoobi et al., A combined experimental and crystal plasticity study of grain size effects in magnesium alloys, Journal of Magnesium and Alloys, https://doi.org/10.1016/j.jma.2023.05.008

Table 1
List of slip direction and slip plane orientations for different slip/twin systems for Mg alloys.

Slip/Twin System	ID	Slip Direction	Slip Plane
Basal	1	$[11\bar{2}0]$	(0001)
	2	$[\bar{2}110]$	(0001)
	3	$[1\bar{2}10]$	(0001)
Prismatic<a>	4	$[1\bar{2}10]$	$(10\bar{1}0)$
	5	$[2\bar{1}\bar{1}0]$	$(01\bar{1}0)$
	6	$[11\bar{2}0]$	$(\bar{1}100)$
Pyramidal<c + a>	7	$[\bar{1}\bar{1}23]$	$(11\bar{2}2)$
	8	$[1\bar{2}13]$	$(\bar{1}2\bar{1}2)$
	9	$[2\bar{1}\bar{1}3]$	$(\bar{2}112)$
	10	$[11\bar{2}3]$	$(\bar{1}\bar{1}22)$
	11	$[\bar{1}2\bar{1}3]$	$(1\bar{2}12)$
	12	$[\bar{2}113]$	$(2\bar{1}\bar{1}2)$
Twin<c + a>	13	$[\bar{1}011]$	$(10\bar{1}2)$
	14	$[10\bar{1}1]$	$(\bar{1}012)$
	15	$[\bar{1}101]$	$(1\bar{1}02)$
	16	$[1\bar{1}01]$	$(\bar{1}102)$
	17	$[0\bar{1}11]$	$(01\bar{1}2)$
	18	$[01\bar{1}1]$	$(0\bar{1}12)$

Table 2
Elastic stiffness constants (in GPa) for Mg-4Al alloy [71,72].

	C_{33}	C_{12}	C_{13}	C_{44}
59.4	61.6	25.61	21.44	16.4

distribution for all the cases considered in this study, a maximum relative difference of about 18% was observed, hence motivating the use of methods to extract the 3D grain size distribution. Once these microstructures are generated using DREAM.3D, the relevant information is passed into the MATLAB preprocessor script to compute d^{α} and k_{μ}^{α} for all voxels constituting the microstructure, using the procedure described in Section 2.2.

2.4.2. Constitutive parameters

All crystal plasticity simulations were performed considering the activity of 12 slip systems; 3 basal, 3 prismatic, 6 pyramidal <c+a>, and 6 extension twin systems (Table 1). Table 2 lists the elastic stiffness constants used in calibration [71,72]. In the hardening law, the latent hardening coefficient was set to $q = 1.0$, while the flow rule parameters were $\dot{\gamma}_0 = 0.001$ and $m = 34$. The plastic constitutive parameters are included in Section 3.1 which covers the calibration of these parameters along with a comparison of stress-strain curves against some of the parameters obtained from localized pile-up stress measurements and parametric curve fitting [49,50].

3. Results and discussion

3.1. Original vs calibrated parameters

Synthetic microstructures were generated for Texture 1 and Texture 2 for three different grain size distributions. For each texture and grain size case, DREAM.3D was fed the input texture and lognormal distribution parameters to generate a microstructure represented as a 50 × 50 × 50 voxelated grid containing approximately 500 grains. In the current work, the experimental data have been divided into two sets for model calibration and model validation. The calibration data set includes the stress-strain curves from microstructures with three grain size distributions with *Texture 1* deformed along the z-direction under tension with periodic boundary constraints to a strain of 1%. The micro Hall-Petch exponents for basal and prismatic systems were kept constant during the calibration. Additionally, since a micro Hall-Petch model for twinning hasn't been developed, a basic Hall-Petch modification of the twinning resistance is considered. Here, the slip resistance for twinning, s^t, is assumed to be of the form $s^t = s_0^t + \frac{K^t}{\sqrt{d_{eq}}}$, where d_{eq} is the mean equivalent grain diameter, which is a single number for a particular microstructure. Table 3 presents the calibrated crystal plasticity parameters using the calibrated data set of *Texture 1* with three different grain sizes. Fig. 5(a) shows that the stress-strain curves obtained by CPFE simulations compare well with those of the experiments for the calibration data set.

In the next step, the predictability of the model is evaluated using the validation data sets, which include microstructures with three grain size distributions with *Texture 2* subjected to two different loading conditions of tension along the z-direction up to a strain of 0.35% and tension along x-direction up to a strain of 1%, both with periodic boundary constraints. Figs. 5(b) and (c) depict the stress-strain curve comparison between CPFE simulations and experiments for all six validation cases. In the case of samples with *Texture 2* subjected to uniaxial tensile deformation along z-axis, Fig. 5(b) shows that although some discrepancies are observed for the initial yielding behavior between the calibrated model and experiment, the CPFE model can predict the stress-strain for strains larger than ~0.2% reasonably well. In the case of samples with *Texture 2* subjected to uniaxial tensile deformation along x-axis, Fig. 5(c) shows a similar discrepancy for the initial yielding behavior. However, the calibrated model successfully predicts the response for strains larger than ~0.55%. This is the first step towards developing a predictive CPFE model to incorporate not only the grain size, but also the grain boundary information along with the grain shape.

Figs. 6(a)-(c) show the yield strength (σ_Y) plotted against the corresponding inverse square-root of grain size ($1/\sqrt{d}$) based on the simulations with the calibrated parameters. The yield strength, σ_Y, for all cases is defined as the 0.2% offset, and the Hall-Petch intercept, σ_0 and Hall-Petch slope, K_{HP} are the intercept and slope, respectively, of the corresponding linear least-squares fit from σ_Y vs $1/\sqrt{d}$ dataset. Additionally, in the σ_Y vs $1/\sqrt{d}$ plots, d refers to the grain area average grain size computed from the corresponding 2D dataset, since this is the measure of grain size that has been traditionally used in such plots due to the availability of only the 2D grain size information. Table 4 shows the comparison between the Hall-Petch coefficients, i.e., the Hall-Petch intercept (σ_0) and Hall-Petch slope (K_{HP}) for all three texture-loading direction

Please cite this article as: A. Lakshmanan, M.T. Andani, M. Yaghoobi et al., A combined experimental and crystal plasticity study of grain size effects in magnesium alloys, Journal of Magnesium and Alloys, https://doi.org/10.1016/j.jma.2023.05.008

Table 3
Crystal plasticity constitutive model parameters post-calibration.

Mode	s_0^α (MPa)	h_0^α (MPa)	s_s^α (MPa)	a^α	K_μ^α $(MPa\ \mu m^{0.5})$	c^α
Basal $<a>$	9.3	300	150	1.0	60	0.6
Prismatic $<a>$	51	600	150	1.0	1000	1.07
Pyramidal $<c+a>$	140	0	200	1.0	0	0
Twin $<c+a>$	17.5	500	100	1.0	25	0

Table 4
Comparison of Hall-Petch coefficients between CPFE simulations and experiments with calibrated parameters.

Hall-Petch coefficients	Texture 1: Exp.	Texture 1: CPFE	Texture 2, z-direction loading: Exp.	Texture 2, z-direction loading: CPFE	Texture 2, x-direction loading: Exp.	Texture 2, x-direction loading: CPFE
σ_0 (MPa)	110.06	112.59	37.66	37.52	97.44	91.84
K_{HP} (MPa $\mu m^{0.5}$)	372.42	308.36	69.44	68.96	254.62	200.52

Table 5
Original parameters which includes the basal and prismatic slip resistances and micro Hall-Petch multipliers [49,50]. The rest of the parameters are set identical to Table 3 for all the simulations with original parameters.

Mode	s_0^α (MPa)	h_0^α (MPa)	s_s^α (MPa)	a^α	K_μ^α $(MPa\ \mu m^{0.5})$	c^α
Basal $<a>$	4.34	300	150	1.0	159	0.6
Prismatic $<a>$	42.54	600	150	1.0	699	1.07
Pyramidal $<c+a>$	140	0	200	1.0	0	0
Twin $<c+a>$	17.5	500	100	1.0	25	0

Table 6
Comparison of Hall-Petch coefficients between CPFE simulations with original parameters and experimental values.

Hall-Petch coefficients	Texture 1: Exp.	Texture 1: CPFE	Texture 2, z-direction loading: Exp.	Texture 2, z-direction loading: CPFE	Texture 2, x-direction loading: Exp.	Texture 2, x-direction loading: CPFE
σ_0 (MPa)	110.06	91.02	37.66	30.55	97.44	73.06
K_{HP} (MPa $\mu m^{0.5}$)	372.42	267.96	69.44	120.07	254.62	216.77

cases between experiments and CPFE simulations with the calibrated parameters.

Figs. 7(a)-(c) present the stress-strain curve comparison between CPFE simulations and experiments for all nine cases considered 3 texture-loading pairs and 3 grain size distributions, with the original parameters extracted from the experiment [49,50] (Table 5). The only parameters modified compared to the calibrated parameters presented in Table 3 are the basal and prismatic slip resistances and micro Hall-Petch multipliers, while the rest of the parameters are identical to the calibrated parameters in Table 3. It is interesting to note that even though the stress-strain curves don't all match with a single parameter set, they produce quite reasonable stress-strain curves. This is especially because the slip resistance values used here were fed to dislocation pile-up models, and the micro Hall-Petch coefficients were then obtained from localized pile-up stress measurements ahead of slip bands blocked by grain boundaries. Figs. 8(a)-(c) show the yield strength (σ_Y) plotted against the corresponding inverse square-root of grain size ($1/\sqrt{d}$) based on the simulations with the original parameters. Table 6 shows the comparison between the Hall-Petch coefficients, i.e., the Hall-Petch intercept (σ_0) and Hall-Petch slope (K_{HP}) for the three texture-loading direction cases between experiments and CPFE simulations with the original parameters.

We note that the calibrated values of the basal and prismatic slip resistances and micro Hall-Petch multipliers (Table 3) are not in agreement with the original values (Table 5). The calibrated basal slip resistance is about twice that of the original basal slip resistance, which was adopted from Akhtar et al. [73] who studied the substitutional solution hardening of magnesium single crystals with different alloying elements. The higher calibrated value indicates additional factors contributing to the initial slip resistance (without size effect contribution) possibly stemming from the underlying defect microstructure in the polycrystalline sample. The calibrated prismatic slip resistance is, however, not very different from original prismatic slip resistance because the original values were estimated from yield strength of polycrystalline stress-strain curves rather than studies on single crystals.

The calibrated basal micro Hall-Petch multiplier is about 0.4 times that of the original basal micro Hall-Petch multiplier obtained from localized measurements of the pile-up stress ahead of blocked slip bands and parametric curve fitting. Here it is important to note that the original basal micro Hall-Petch multiplier was obtained by fitting the micro Hall-

Please cite this article as: A. Lakshmanan, M.T. Andani, M. Yaghoobi et al., A combined experimental and crystal plasticity study of grain size effects in magnesium alloys, Journal of Magnesium and Alloys, https://doi.org/10.1016/j.jma.2023.05.008

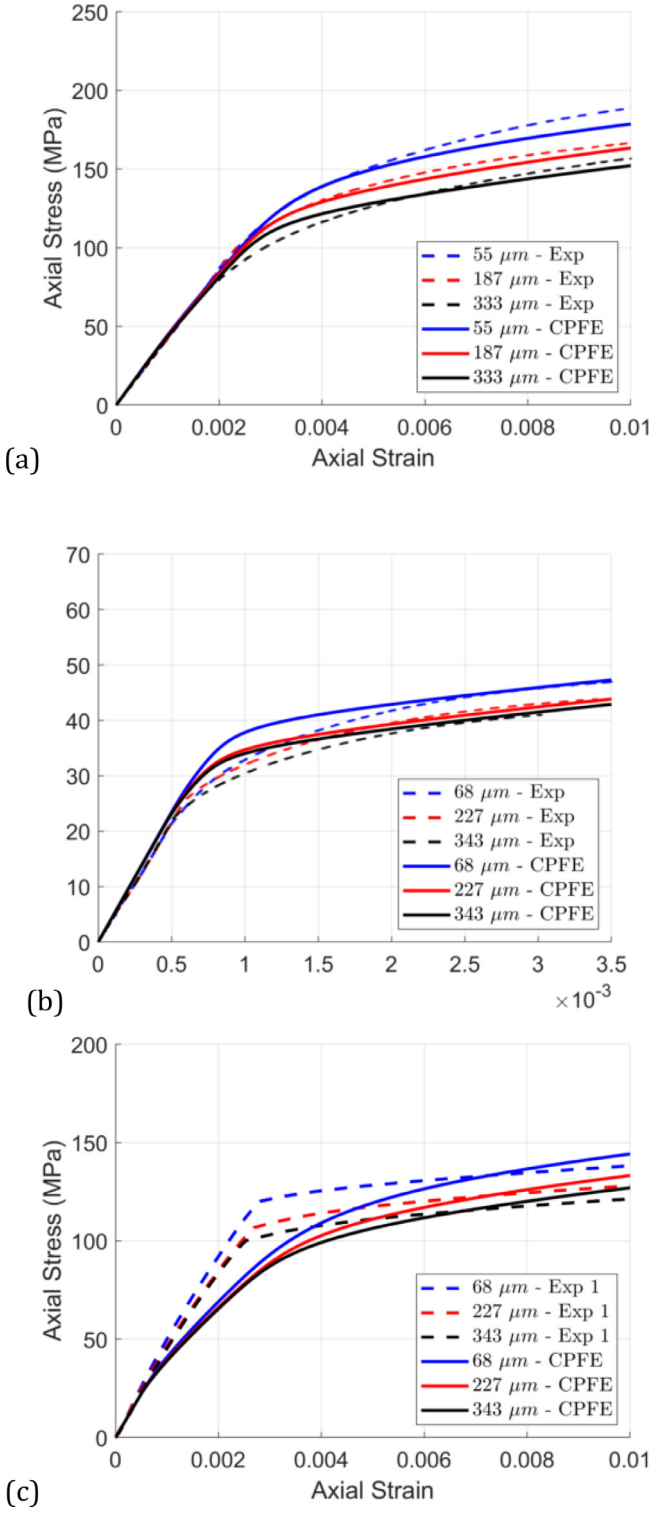

Fig. 5. Stress-strain curve comparison between CPFE simulations and experiments using calibrated parameters for (a) Texture 1, z-direction tensile loading, (b) Texture 2, z-direction tensile loading and (c) Texture 2, x-direction tensile loading.

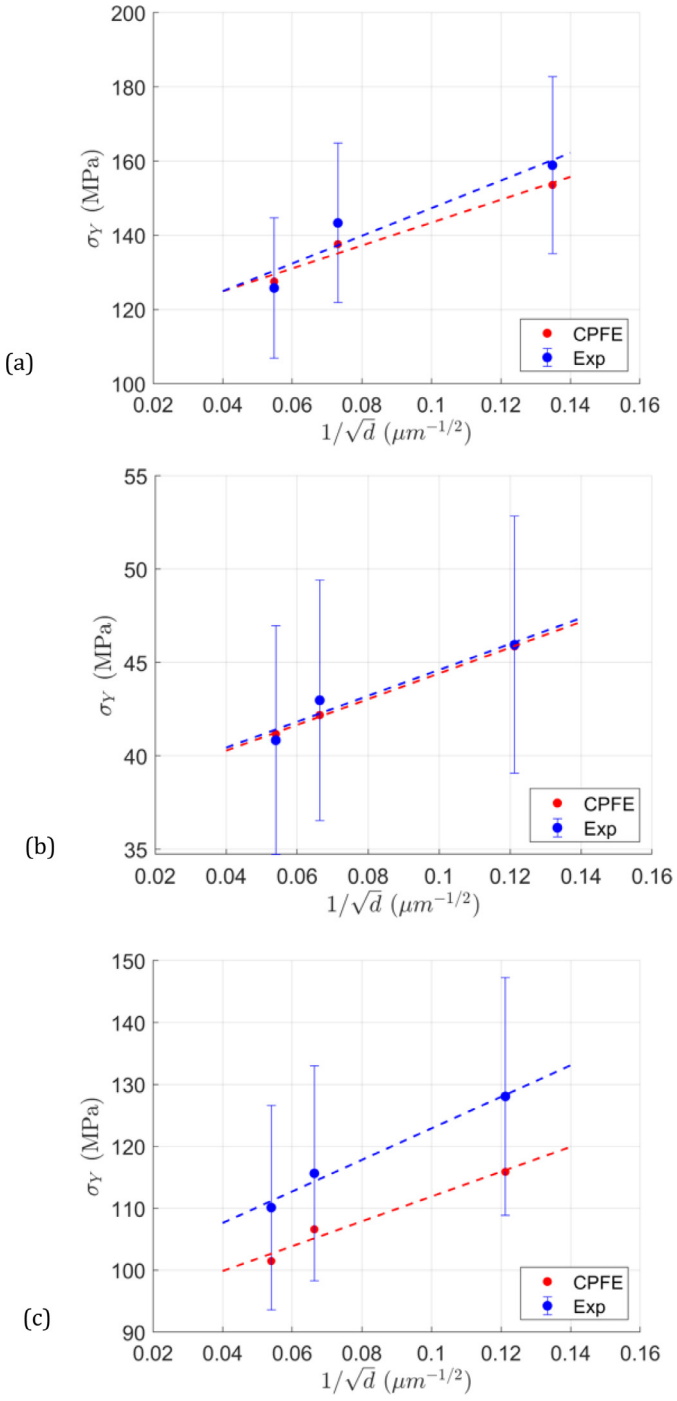

Fig. 6. Yield strength (σ_Y) with error bars vs inverse square-root grain size ($1/\sqrt{d}$) comparison between CPFE simulations and experiments using calibrated parameters for (a) Texture 1, z-direction tensile loading, (b) Texture 2, z-direction tensile loading and (c) Texture 2, x-direction tensile loading. Dotted lines denote corresponding linear-fit.

Petch parameters for eight grain boundaries to a power-law type function of the maximum compatibility factor. The micro Hall-Petch parameters for those eight grain boundaries were obtained by fitting pile-up stress measurements ahead of a blocked slip band, to expressions obtained from a continuum dislocation pile-up model. On the other hand, the crystal plas-

Please cite this article as: A. Lakshmanan, M.T. Andani, M. Yaghoobi et al., A combined experimental and crystal plasticity study of grain size effects in magnesium alloys, Journal of Magnesium and Alloys, https://doi.org/10.1016/j.jma.2023.05.008

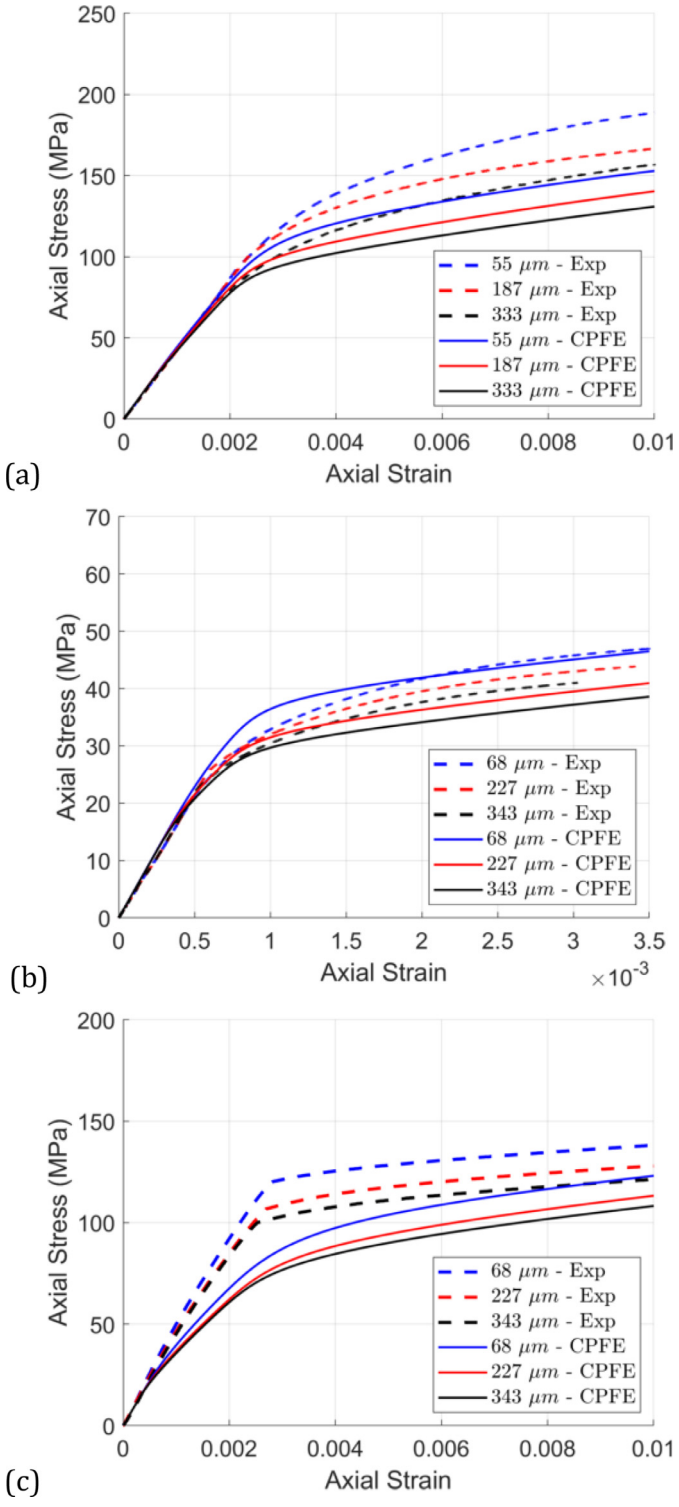

Fig. 7. Stress-strain curve comparison between CPFE simulations and experiments using original parameters for (a) Texture 1, z-direction tensile loading, (b) Texture 2, z-direction tensile loading and (c) Texture 2, x-direction tensile loading.

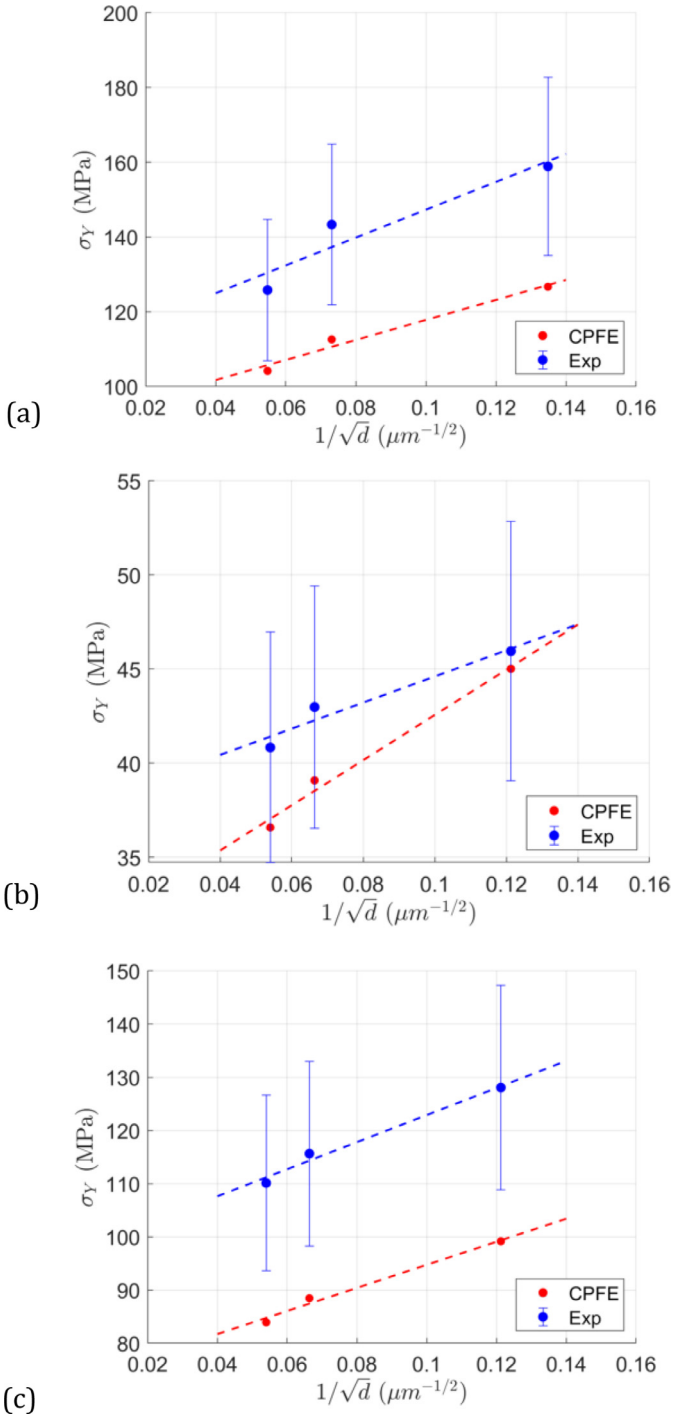

Fig. 8. Yield strength (σ_Y) with error bars vs inverse square-root grain size ($1/\sqrt{d}$) comparison between CPFE simulations and experiments using original parameters for (a) Texture 1, z-direction tensile loading, (b) Texture 2, z-direction tensile loading and (c) Texture 2, x-direction tensile loading. Dotted lines denote corresponding linear-fit.

ticity finite element simulation forms a homogenized representation of the microstructure where a large number of points in the simulated microstructure accommodate slip as opposed to localized slip bands in experiments. Since all microstructural points in the synthetic microstructures are endowed with a micro Hall-Petch coefficient and an underlying slip system-

Please cite this article as: A. Lakshmanan, M.T. Andani, M. Yaghoobi et al., A combined experimental and crystal plasticity study of grain size effects in magnesium alloys, Journal of Magnesium and Alloys, https://doi.org/10.1016/j.jma.2023.05.008

level grain size, this implies that a lower value of the basal micro Hall-Petch multiplier is sufficient to capture the contribution of basal slip to the grain size effect. We additionally note that if not all microstructural points but only select number were endowed with the basal micro Hall-Petch multiplier, the calibrated basal micro Hall-Petch multiplier will increase and be closer to the original basal micro Hall-Petch multiplier.

In contrast, the calibrated prismatic micro Hall-Petch multiplier is about 1.4 times that of the original prismatic micro Hall-Petch multiplier obtained from localized measurements of the pile-up stress ahead of blocked slip bands and parametric curve fitting. Here again the original prismatic micro Hall-Petch multiplier was obtained by fitting the micro Hall-Petch parameters for seven grain boundaries to a power-law type function of the maximum compatibility factor. The micro Hall-Petch parameters for those seven grain boundaries were obtained by fitting pile-up stress measurements ahead of a blocked slip band (initiated from a notch within a grain), to expressions obtained from a continuum dislocation pile-up model. In this case, the implication is that even with a homogenized model like crystal plasticity where each microstructural point has a contribution to the size effect, a relatively higher prismatic micro Hall-Petch multiplier is necessary to capture the grain size effect. In other words, the effect of grain boundaries on prismatic slip is possibly more profuse when analyzing many different boundaries as compared to just the seven boundaries.

We also note that the implementation of the micro Hall-Petch constitutive model accounts for the maximum compatibility factor purely dependent on the orientation of neighboring grains without accounting for grain boundary inclination, which is not very straightforward to account for universally because it is dependent on the underlying mesh used for computational studies. However, if a possible standardization can be achieved in the inclusion of grain boundary information across microstructure generation frameworks, then this information can be included without much additional effort providing better insights and possibly even better agreement between calibration parameters and experimentally informed parameters. Next, we carry out some simple parametric studies with the calibrated parameters to explore different examples where the grain size and texture are coupled.

3.2. Effect of simulated spread in texture

Here we simulate and study the behavior of the Hall-Petch slope for microstructures whose crystallographic textures are represented by predominantly basal texture superposed with a spread in orientations. This spread is representative of orientations spreading almost uniformly, away from the basal poles. The purpose of this study with simulated orientation spread alludes to the fact that different processing routes result in different textures, which in turn affect the mechanical properties.

All the microstructures used in this study were generated using DREAM.3D in which the respective textures were created by specifying the Euler angle (Bunge convention) triplet of (0, 0, 0) with a weight equal to 100 and spread (denoted by ε) equal to a positive value denoting the respective spread in the orientations. For each texture, a base microstructure was first generated for the smallest grain size using the lognormal distribution parameters corresponding to the smallest grain size for Texture 2. This base microstructure was then uniformly scaled to twice, thrice and four times its size, to generate geometrically similar microstructures with different grain sizes. For a measure of the average 2D grain size, we directly use the grain area average grain size of the experimental 2D microstructure from which the 3D lognormal distribution parameters were obtained. Then for the smallest grain size case, the grain area average grain size is 68 μm, and accordingly, 136 μm, 204 μm and 272 μm for the microstructures scaled to twice, thrice and four times the smallest size, respectively. Additionally, to better represent the underlying texture, microstructures with larger number of grains were created for the textures corresponding to $\varepsilon = 20$, $\varepsilon = 23$ and random texture. Figs. 9a-9i depict the pole figures generated for different values of the spread considered, denoted by the ε value, along with the approximate number of grains contained in the synthetic microstructure for that texture.

Simulations were performed in which the microstructures were deformed in tension along the z-direction to 1% strain, with periodic boundary constraints. Fig. 10a shows the plots of the predicted yield strength (σ_Y) vs inverse square-root of grain size ($1/\sqrt{d}$) for the different textures from which a linear least-squares fit (denoted by dotted line) yields the Hall-Petch intercept and the Hall-Petch slope (Fig. 10c). Here d denotes the measure of average 2D grain size noted earlier. Fig. 10b depicts the variation of the size-dependent component of the yield strength for the different textures and grain sizes to better visualize the Hall-Petch slope. The Hall-Petch slope increases progressively from 49 $MPa\,\mu m^{0.5}$ for $\varepsilon = 5$ to 79 $MPa\,\mu m^{0.5}$ for $\varepsilon = 23$, close to the Hall-Petch slope for random texture at about 93 $MPa\,\mu m^{0.5}$. First a gradual increase is observed from 49 $MPa\,\mu m^{0.5}$ for $\varepsilon = 5$ to 58 $MPa\,\mu m^{0.5}$for $\varepsilon = 15$, after which the increase is more drastic to 79 $MPa\,\mu m^{0.5}$ for $\varepsilon = 23$.

A measure of the slip activity of different slip system families is investigated to better understand the observed behavior. Fig. 11 shows the average accumulated slip on the basal, prismatic and twin systems at the end of deformation for the smallest grain size. The average accumulated slip for a particular slip system type (basal, prismatic or twin) is computed by averaging the total slip contribution of all slip systems associated with that slip system type, over the entire microstructure. For example, for the basal system the total slip contribution from the three basal slip systems is computed for all points in the microstructure, and then the mean is taken over all those microstructural points.

The Hall-Petch slope is a reflection of the activity of individual slip systems, since even physically, slip has to ensue on individual slip systems for the effect of the grain boundaries (or alternatively the grain size) to be felt. As the spread increases from $\varepsilon = 5$ to $\varepsilon = 15$, there is an increase in the average basal accumulated slip and a decrease in the average

Please cite this article as: A. Lakshmanan, M.T. Andani, M. Yaghoobi et al., A combined experimental and crystal plasticity study of grain size effects in magnesium alloys, Journal of Magnesium and Alloys, https://doi.org/10.1016/j.jma.2023.05.008

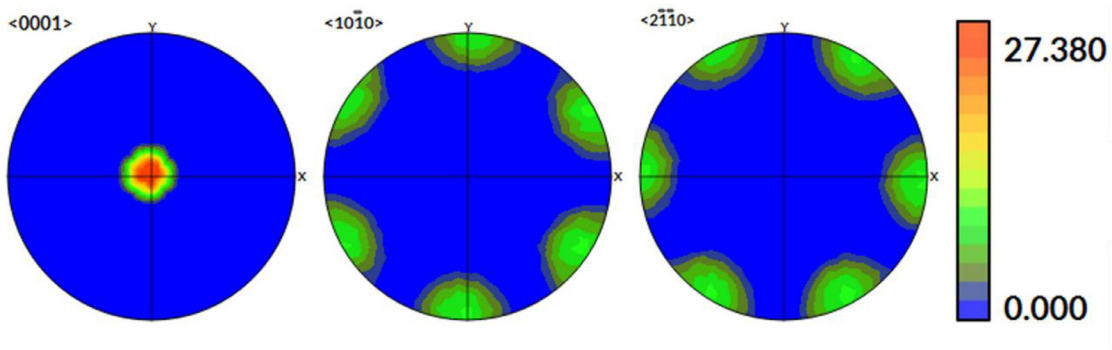

(a) ϵ = 5, approx. 500 grains

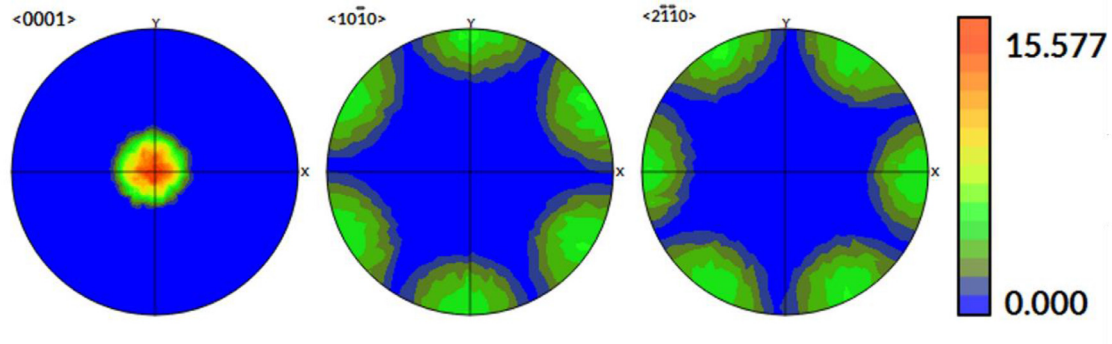

(b) ϵ = 7, approx. 500 grains

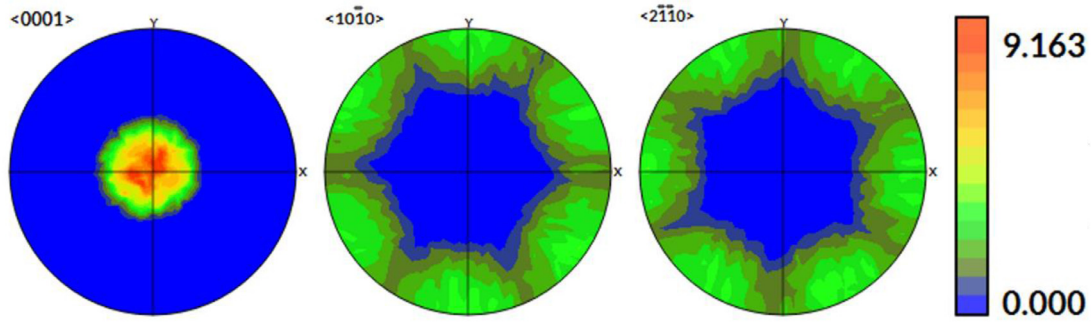

(c) ϵ = 9, approx. 500 grains

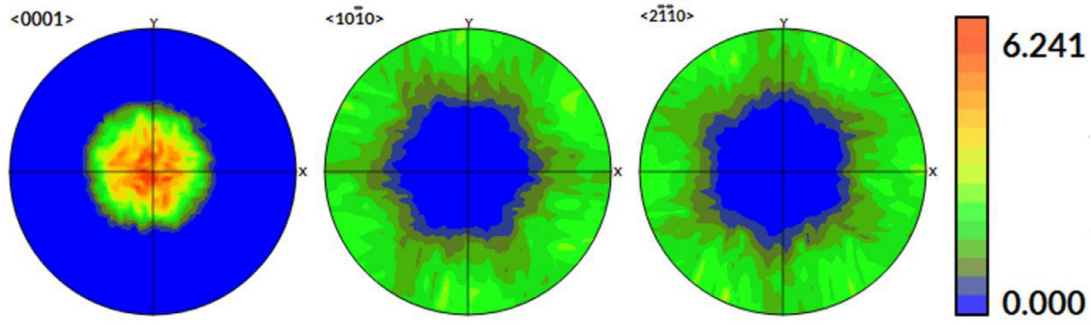

(d) ϵ = 11, approx. 500 grains

Fig. 9. Pole figures for increasing values of the ε value or spread in orientations and the approximate number of grains constituting the synthetic microstructure. Since, random texture corresponds to a uniform distribution of orientations, the pole figures were not generated in the same manner as the previous pole figures. Instead, a sample of random orientations was created using MTEX and specified as input to DREAM.3D.

Please cite this article as: A. Lakshmanan, M.T. Andani, M. Yaghoobi et al., A combined experimental and crystal plasticity study of grain size effects in magnesium alloys, Journal of Magnesium and Alloys, https://doi.org/10.1016/j.jma.2023.05.008

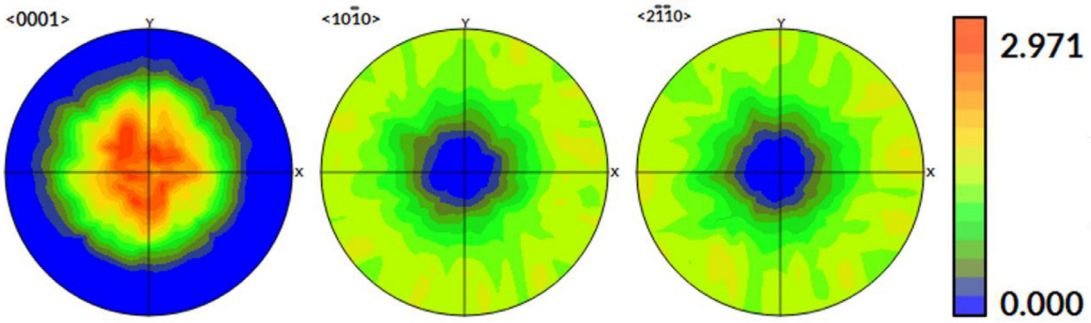

(e) ϵ = 15, approx. 500 grains

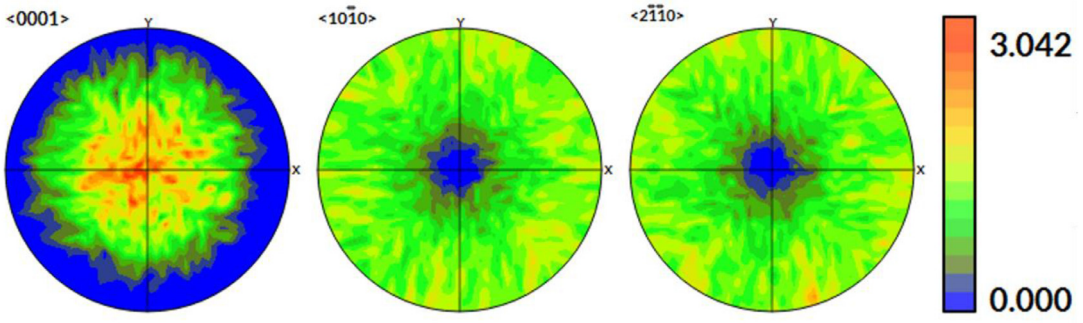

(f) ϵ = 17, approx. 500 grains

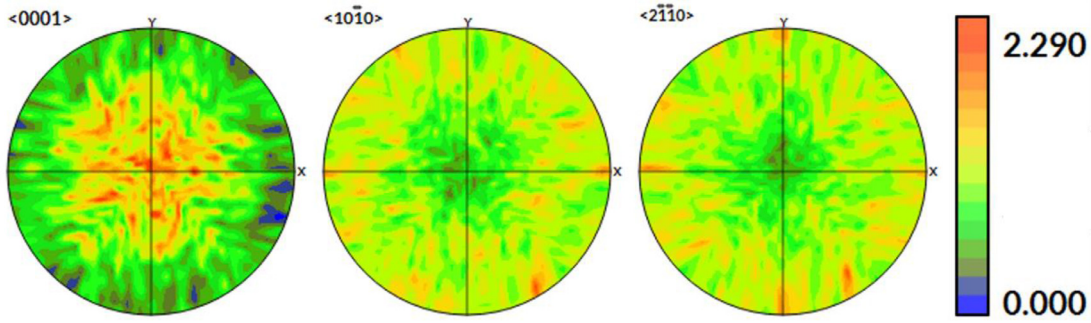

(g) ϵ = 20, approx. 800 grains

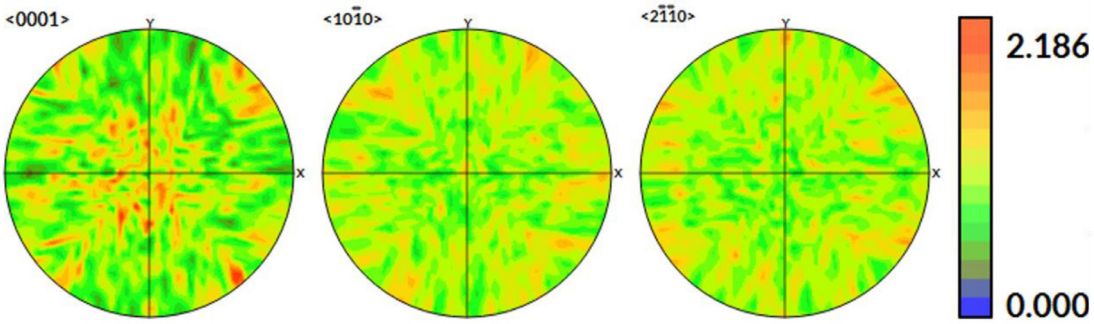

(h) ϵ = 23, approx. 1300 grains

Fig. 9. Continued

Please cite this article as: A. Lakshmanan, M.T. Andani, M. Yaghoobi et al., A combined experimental and crystal plasticity study of grain size effects in magnesium alloys, Journal of Magnesium and Alloys, https://doi.org/10.1016/j.jma.2023.05.008

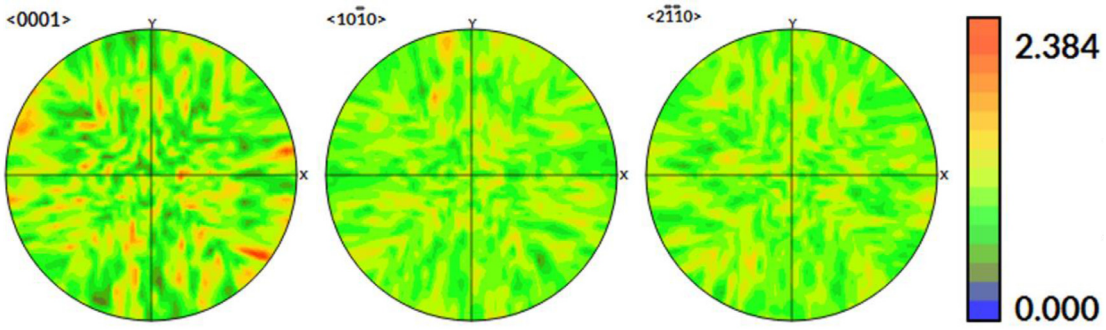

(i) Random texture, approx. 1300 grains

Fig. 9. Continued

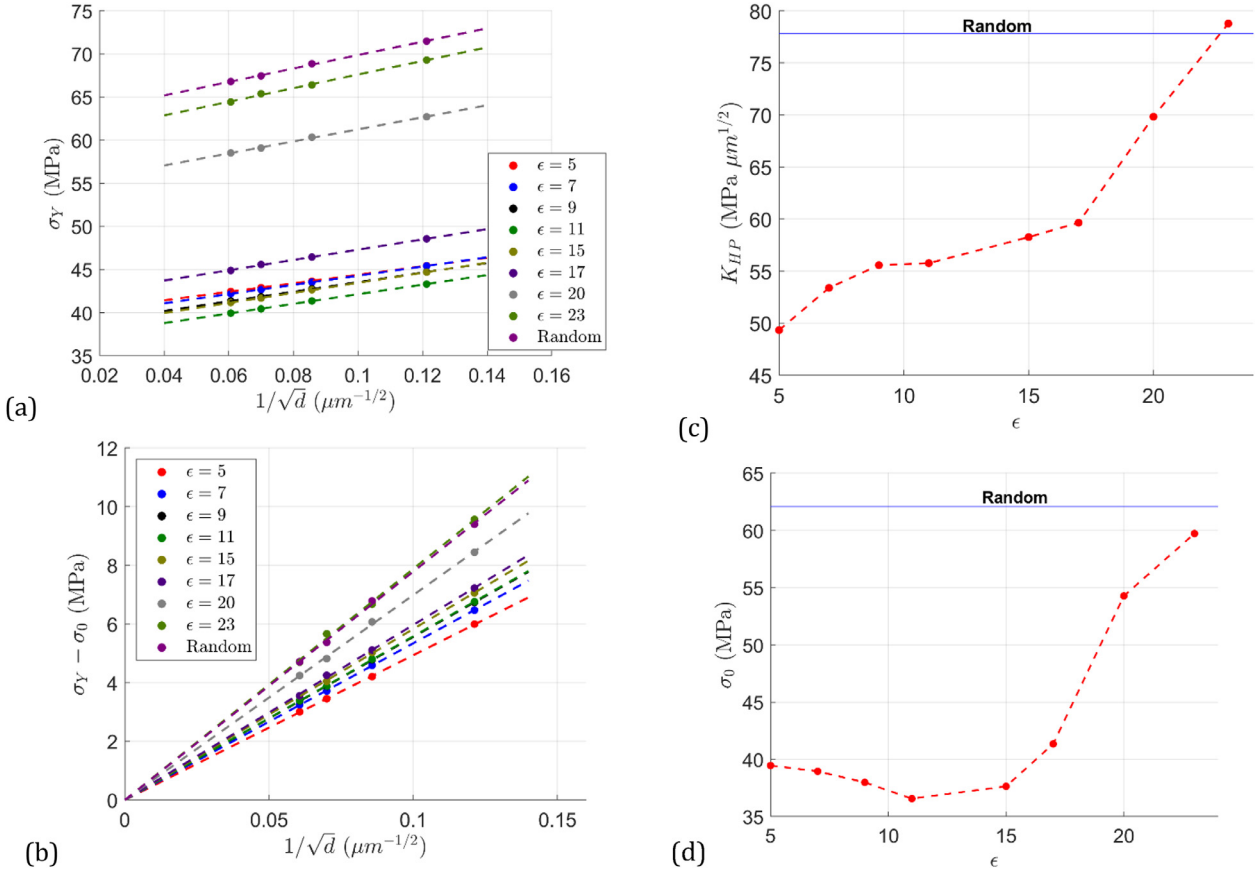

Fig. 10. (a) Predicted yield strength (σ_Y) vs inverse square-root grain size ($1/\sqrt{d}$) for different spreads of basal texture, and random texture. Dotted lines denote corresponding linear least-squares fit. (b) Size-dependent contribution of yield strength to visualize difference in Hall-Petch slopes, (c) Hall-Petch slope for different ε values, (d) Hall-Petch intercept for different ε values.

twin accumulated slip. Note that for twinning there does not exist a maximum compatibility factor when accounting for the size-dependent contribution to the slip resistance, while for the basal systems the micro Hall-Petch coefficient is multiplied with a power-law type function of the maximum compatibility factor. Additionally, for twinning there is a single average grain size used in the expression to modify the slip resistance, while for basal systems the slip system-level grain size, which is a heterogeneous property, comes into play. As a result, while the effect of twinning is almost homogeneous across all points where twinning accommodates deformation, that is not the case for basal slip which shows a larger spread in its contributions. Then there are two competing factors – (i) The decrease in twinning activity with an increase in ε which reduces the contribution of twinning to the Hall-Petch slope, while (ii) Increased basal activity combined with a spread in texture increases basal contribution to the Hall-Petch slope due to delocalization of texture – more diffuse texture =>

Please cite this article as: A. Lakshmanan, M.T. Andani, M. Yaghoobi et al., A combined experimental and crystal plasticity study of grain size effects in magnesium alloys, Journal of Magnesium and Alloys, https://doi.org/10.1016/j.jma.2023.05.008

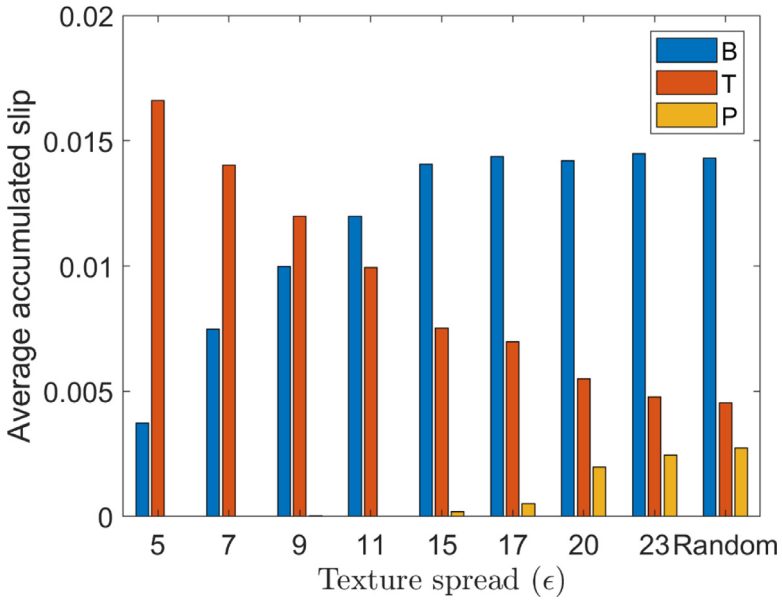

Fig. 11. Comparison of average accumulated slip on basal, prismatic and twin systems at the end of deformation for different values of the spread ε. The average accumulated slip for a particular slip system type is computed by averaging the total slip contribution of all slip systems associated with that slip system type, over the entire microstructure. B – Basal, P – Prismatic, T – Twin.

lower values of maximum compatibility factor => increased contribution of basal slip to the grain size effect. The increase in the Hall-Petch slope signifies the dominance of increased basal slip activity over twinning activity as we go from sharper texture for $\varepsilon = 5$ to more diffuse texture for $\varepsilon = 15$. Beyond $\varepsilon = 15$ the Hall-Petch slope increases and this can be attributed to further delocalization of texture and the activation of prismatic systems, which have a relatively high micro Hall-Petch coefficient compared to basal system. Even though prismatic slip systems don't show significant activity, combining the high micro Hall-Petch coefficient of prismatic slip with smaller values maximum compatibility factor and increased prismatic slip activity ensures a steady increase in the Hall-Petch slope as the texture approaches random texture. The variation of σ_0 which is predominantly dictated by the texture, can be explained by the accumulated slip plot. The lower values of σ_0 for lower values of ε is attributed to the presence of only basal and twin activity, both of which possess much lower slip resistance relative to the prismatic systems. The decrease in σ_0 up to $\varepsilon = 11$ is attributed to the increased activity of basal and decreased activity of twin, combined with the facts that basal slip resistance is lower than twinning and there is no prismatic activation. The subsequent increase in σ_0 beyond $\varepsilon = 11$ is attributed to the increase in prismatic activity which becomes the dominant deformation mechanism in the face of lower twinning activity, while basal activity remains almost unaltered.

3.3. Effect of loading direction

In this section, we study computationally the Hall-Petch slope of microstructures with sharp basal texture relative to the angle φ, made between the loading direction and direction of basal poles. This is in principle very similar to the experimental study presented by Wang et al. [20] which was performed for Mg-AZ31 alloy with a more diffuse basal texture. Similar to that study, we consider five values of φ – 0°, 22.5°, 45°, 67.5°and 90° For each φ, a microstructure was first generated for the smallest grain size using the lognormal distribution parameters corresponding to the smallest grain size for Texture 2. This microstructure was then uniformly scaled to twice, thrice and four times its size, hence generating the same microstructure with different grain sizes. Similar to the previous study, for the smallest grain size case, the grain area average grain size is taken to be 68 μm, and accordingly, 136 μm, 204 μm and 272 μm for the microstructures scaled to twice, thrice and four times the smallest size, respectively. Each microstructure was constructed as a 50 × 50 × 50 voxelated grid with approximately 500 grains. The synthetic microstructures were then deformed in tension along z-direction to a strain of 1% with periodic boundary constraints.

Fig. 12a depicts the pole figures representing the orientation distribution based on which the synthetic microstructures were generated for this study. Fig. 12b depicts the plots of the yield strength (σ_Y) vs inverse square-root of grain size ($1/\sqrt{d}$) for different φ, from which a linear least-squares fit (denoted by dotted line) yields the Hall-Petch intercept and Hall-Petch slope (Fig. 12d). Here d denotes the measure of average 2D grain size noted earlier. Fig. 12c depicts the variation of the size-dependent component of the yield strength with inverse square-root of grain size for the different φ.

A very interesting behavior is observed here where the Hall-Petch slope first decreases to a minimum at $\varphi = 45^o$ after which it increases again to $\varphi = 90^o$. Fig. 13 shows the average accumulated slip on the basal, prismatic and twin systems at the end of deformation for the smallest grain size. As φ

Please cite this article as: A. Lakshmanan, M.T. Andani, M. Yaghoobi et al., A combined experimental and crystal plasticity study of grain size effects in magnesium alloys, Journal of Magnesium and Alloys, https://doi.org/10.1016/j.jma.2023.05.008

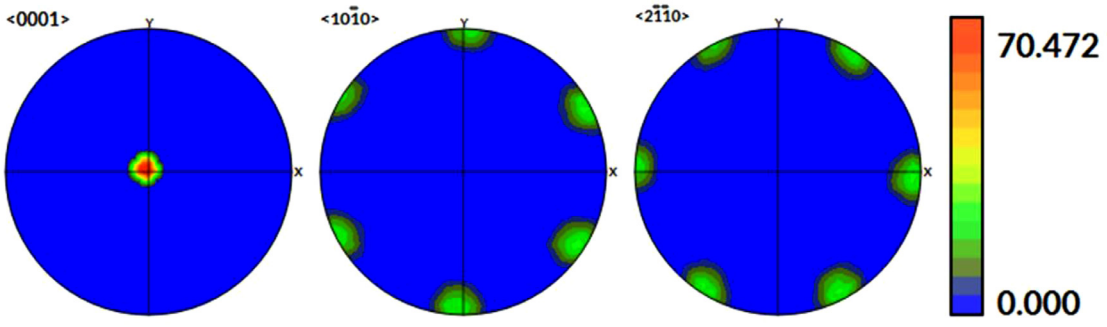

(a)

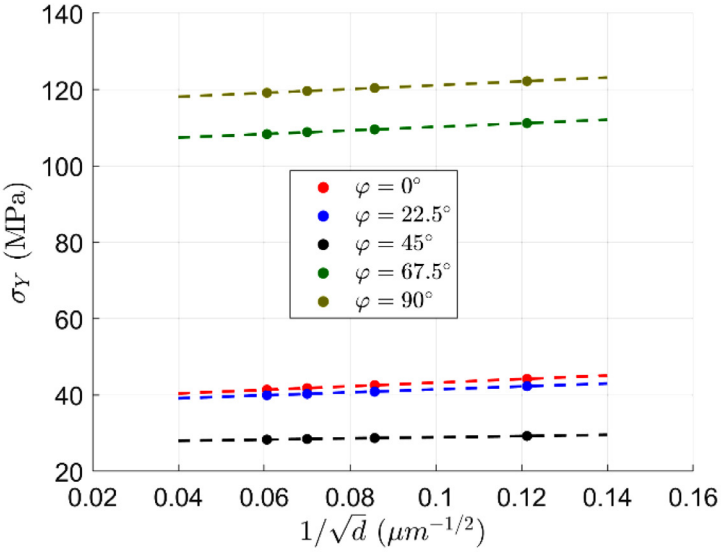

(b)

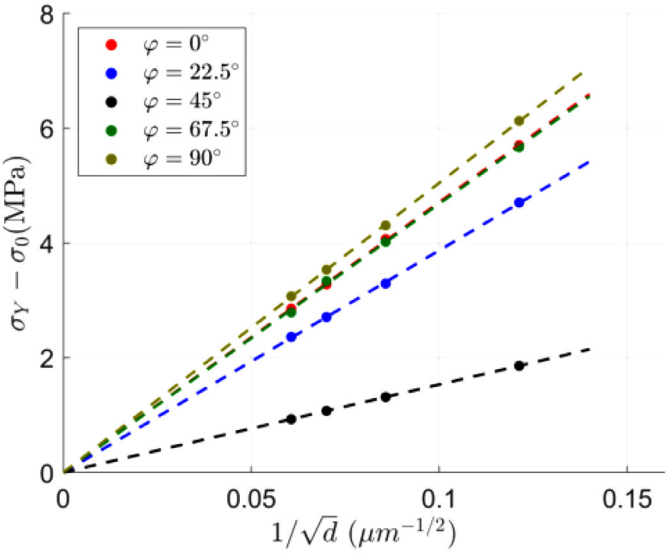

(c)

Fig. 12. (a) Pole figures of strong basal texture were used to generate the microstructures for this study. (b) Predicted yield strength (σ_Y) vs inverse square-root grain size ($1/\sqrt{d}$) for different relative loading directions given by φ. Dotted lines denote corresponding linear-fit. (c) Size-dependent contribution of yield strength. (d) Hall-Petch slope plotted for different φ values (e) Hall-Petch intercept plotted for different φ values.

Please cite this article as: A. Lakshmanan, M.T. Andani, M. Yaghoobi et al., A combined experimental and crystal plasticity study of grain size effects in magnesium alloys, Journal of Magnesium and Alloys, https://doi.org/10.1016/j.jma.2023.05.008

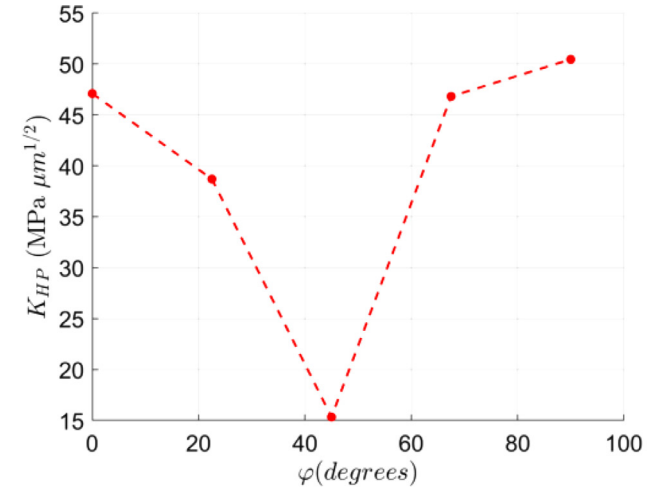

(d)

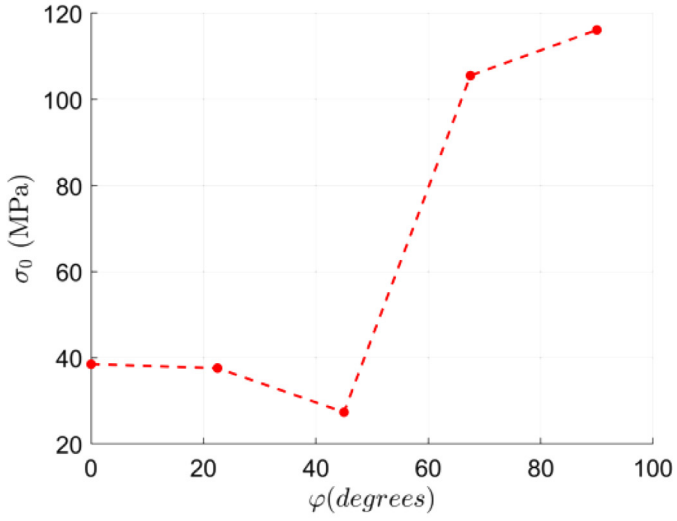

(e)

Fig. 12. Continued

varies from 0^o to 45^o, the activity of basal slip increases while the twinning activity decreases. Unlike the previous parametric study, the texture is the same for different relative angles of loading and the decrease in the effect of twinning activity dominates over the increased basal activity, resulting in a decrease in the Hall-Petch slope from 47 $MPa\,\mu m^{0.5}$ when twinning predominates at 0^o to 15 $MPa\,\mu m^{0.5}$ when basal predominates at 45^o. Subsequently, as φ increases from 45^o to 90^o prismatic activity increases significantly while basal activity decreases and twinning activity remains negligible. Due to the relatively high micro Hall-Petch coefficient of the prismatic system compared to the basal system, the increase in prismatic activity dominates the decrease in basal activity, contributing to the net increase in the Hall-Petch slope from 45^o to 90^o. The variation of σ_0 which is predominantly dictated by the texture, can be explained by the accumulated slip plot. The lower values of σ_0 for φ<45° is attributed to the presence of only basal and twin activity, both of which possess much lower slip resistance relative to the prismatic systems. The decrease in σ_0 for φ<45° is attributed to the increased activity of basal and decreased activity of twinning, combined with the facts that basal slip resistance is lower than twinning and there is no prismatic activation. The subsequent significant increase in σ_0 beyond φ=45° is attributed to the increase in prismatic activity in the face of no twinning activity and decreasing basal activity.

3.4. Yield strength variation with grain morphology

In this section, we study the variation of the yield strength of simulated microstructures with different grain morphologies with underlying crystallographic texture corresponding to the Texture 1 from experiments (Fig. 3a). First, a microstructure was generated for the smallest grain size using the log-normal distribution parameters corresponding to the smallest grain size. The synthetic microstructure used for this study is a 50 × 50 × 50 voxelated grid consisting of approximately 500 grains. Different morphologies are quantified by the as-

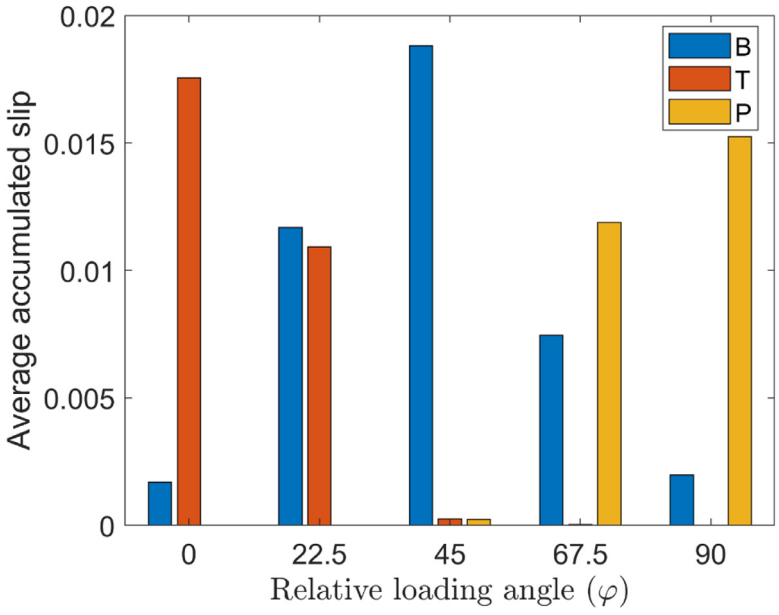

Fig. 13. Comparison of average accumulated slip at the end of deformation for basal, prismatic and twin systems for different angles φ. B – Basal, P – Prismatic, T – Twin.

pect ratio α, which is used to modify the voxel spacings depending on the relative aspect ratios along three orthogonal directions. Let us consider a microstructure containing equiaxed grains with voxel resolutions of Δl along the x, y and z-direction, for which we wish to construct a microstructure with grains possessing an aspect ratio of α. Then the triplet of resolutions for the equiaxed microstructure, (Δl, Δl, Δl) is transformed to the new triplet ($\alpha^{-1/3}\,\Delta l$,$\alpha^{-1/3}\,.\Delta l$,$\alpha^{2/3}\,\Delta l$). This preserves the volume of each voxel and hence the entire grain, as a result preserving the grain size statistics as well. Additionally, the aspect ratio α now corresponds to the ratio of the transformed resolution along the z-direction to that along the x (or y)-direction. This eventually affects the computation of slip system-level grain size and hence the micro Hall-Petch contribution to the slip resistance. Earlier work on incorporating the grain size effect has focused on modifying the slip resistance based on the average grain size alone, which in this case is the same for all microstructures since the grain volumes are preserved. As a result, the morphology of the grains cannot be captured in those models, unlike the present one where the morphology affects the slip system-level grain sizes.

CPFE simulations are performed on the microstructures which are deformed in tension along the z-direction to 1% engineering strain with periodic boundary constraints. Nine different aspect ratios are considered: $\alpha = \frac{1}{5}$, $\alpha = \frac{1}{4}$, $\alpha = \frac{1}{3}$, $\alpha = \frac{1}{2}$, $\alpha = 1$, $\alpha = 2$, $\alpha = 3$, $\alpha = 4$ and $\alpha = 5$. Fig. 14 shows the variation of the yield strength with change in aspect ratio. It is interesting to note that the variation on yield strength is non-monotonic relative to the logarithm of the aspect ratio. To explain this behavior, we obtain the relevant expressions using elementary geometry and some crystallographic and plastic properties particular to as-extruded texture.

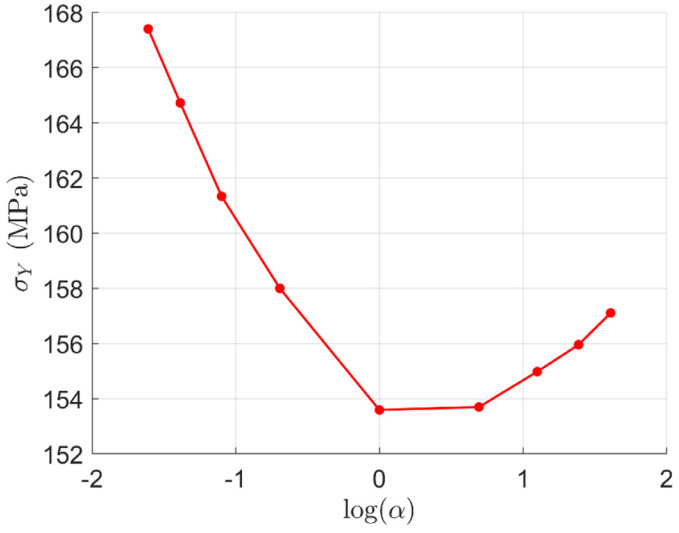

Fig. 14. Yield strength (σ_Y) for different aspect ratios of grains. Note the asymmetry in the yield strength relative to the logarithm of the aspect ratio α.

We first note that the microstructures for different aspect ratios used in this study are generated by uniform stretches along the three orthogonal directions of a microstructure with equiaxed grains. Since equiaxed grains are essentially space filling representations of spheres, the grains in microstructures with aspect ratios different from 1 are prolate or oblate spheroids depending on $\alpha > 1$ or $\alpha < 1$, respectively, with the axis of circular symmetry coinciding with the z-direction. Now consider such an ellipsoid with axes lengths abiding the ratio dictated by the triplet of resolutions used to generate the microstructure. Denote the semi-axes lengths along the x, y and z directions by a, b and c respectively, and let R denote the radius of the sphere representing the equivalent sphere

Please cite this article as: A. Lakshmanan, M.T. Andani, M. Yaghoobi et al., A combined experimental and crystal plasticity study of grain size effects in magnesium alloys, Journal of Magnesium and Alloys, https://doi.org/10.1016/j.jma.2023.05.008

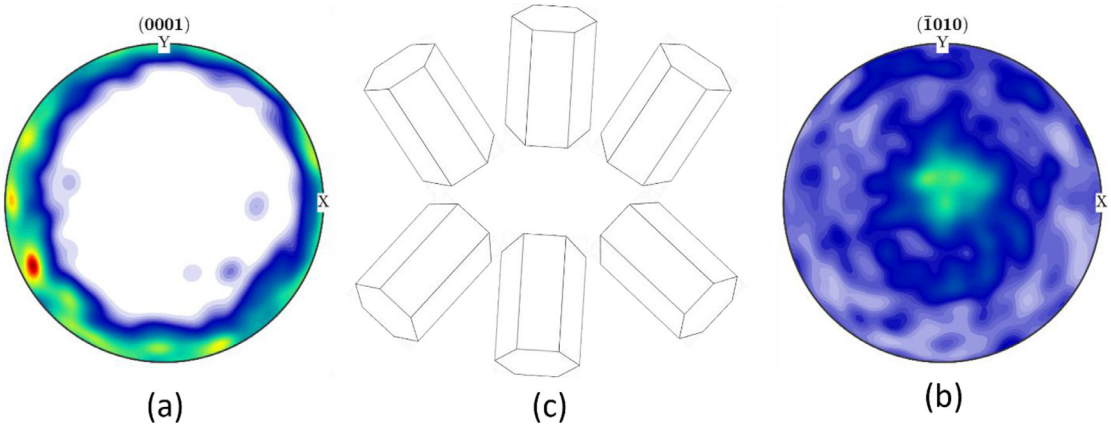

Fig. 15. (a) (0001) pole figure, (b) $(10\bar{1}0)$ pole figure, and (c) theoretical arrangement of HCP unit cells symmetrically about the extrusion direction with the $(10\bar{1}0)$ plane normal pointing along the extrusion direction.

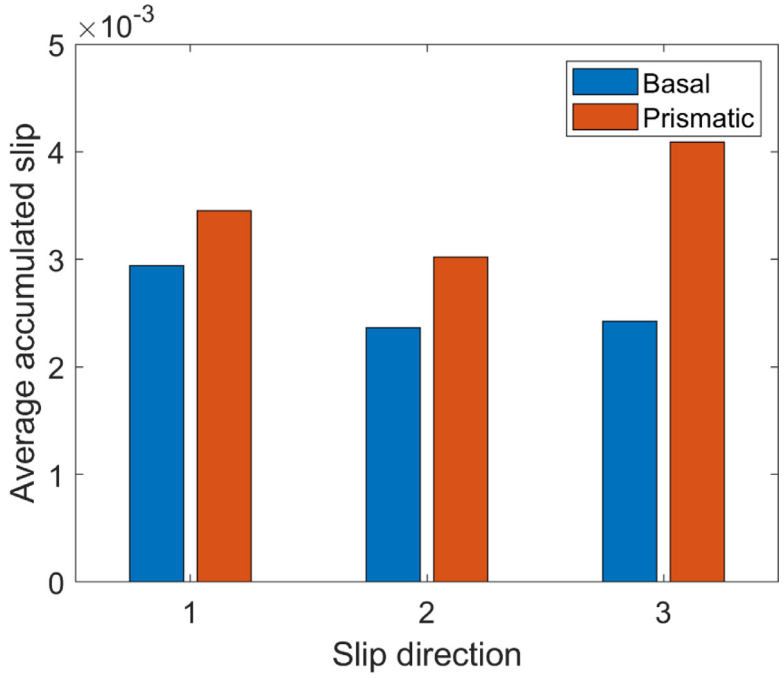

Fig. 16. The average accumulated slip on the three basal and three prismatic slip systems. The integers on the x-direction denote a specific slip direction: '1′ - $[11\bar{2}0]$, '2′ - $[\bar{2}110]$ and '3′ - $[1\bar{2}10]$.

grain diameter of the equiaxed grain from which the ellipsoidal grain was obtained. Then the semi-axes lengths must be $a = \alpha^{-1/3}R$, $b = \alpha^{-1/3}R$ and $c = \alpha^{2/3}R$ resulting in the following equation of the ellipsoid:

$$\frac{x^2}{a^2} + \frac{y^2}{b^2} + \frac{z^2}{c^2} = 1 \Rightarrow \frac{r^2}{\alpha^{-2/3}} + \frac{z^2}{\alpha^{4/3}} = R^2 \tag{18}$$

where $r^2 = x^2 + y^2$. In the context of the as-extruded texture, the $(10\bar{1}0)$ poles are concentrated in the extrusion direction, as seen in the $(10\bar{1}0)$ pole figure. In addition to this, the basal plane normals are aligned perpendicular to the extrusion direction, with almost uniform distribution as evidenced by the close to vertical band in the (0001) pole figure. This suggests a theoretically uniform arrangement of the HCP unit cells about the extrusion direction with the $(10\bar{1}0)$ prismatic plane normal being parallel to the extrusion direction (Fig. 15). From the perspective of plasticity, the basal and prismatic systems are the primary slip systems activated when this texture is deformed along the extrusion direction. Fig. 16 depicts a plot of the percentage contribution to average accumulated slip at the end of deformation by the three individual basal and prismatic slip systems.

Even though there is some difference in the average accumulated slip by slip systems corresponding to different slip directions, let's assume for theoretical purposes that they are equal. In other words, slip systems corresponding to each slip direction contribute equally to the total average accumulated slip due to basal and prismatic systems. This means that among the three slip directions one of them is always perpendicular to the extrusion direction while the remaining two are

Please cite this article as: A. Lakshmanan, M.T. Andani, M. Yaghoobi et al., A combined experimental and crystal plasticity study of grain size effects in magnesium alloys, Journal of Magnesium and Alloys, https://doi.org/10.1016/j.jma.2023.05.008

at 30° to the extrusion direction. In our case, slip direction '1′ is perpendicular to the extrusion direction, while the remaining two directions are at 30° to the extrusion direction. Let's now consider the measure of grain size for a particular slip direction as the length of the line segment passing through the center of the ellipsoid with direction coinciding with the slip direction. Denote this grain size measure for slip direction 'i' by d_i. With knowledge of the slip directions relative to the ellipsoid the grain size measures are straightforward to obtain using Eq. (18):

$$d_1 = \alpha^{-1/3}R;\ \ d_2 = d_3 = \frac{2\mathrm{R}}{\sqrt{3}}\left(\frac{\alpha^{2/3}}{3} + \alpha^{-4/3}\right)^{-1/2} \tag{19}$$

With the earlier assumption of equal contribution of slip from the slip directions, the size-dependent contribution to the yield strength can be expressed as being proportional to the quantity β defined using Eq. (17) with the inverse square-root dependence on grain size measure:

$$\beta := \frac{1}{\sqrt{d_1}} + \frac{1}{\sqrt{d_2}} + \frac{1}{\sqrt{d_3}} = \frac{\delta\ (\alpha)}{\sqrt{\mathrm{R}}} \tag{20}$$

where:

$$\delta\ (\alpha) = \sqrt{\alpha^{1/3}}\ +\ \sqrt{2}\left(\alpha^{2/3}\ +\ 3\alpha^{-4/3}\right)^{1/4} \tag{21}$$

$\delta\,(\alpha)$ encodes the dependence of the yield strength on the aspect ratio α. This function is visualized by plotting it (Fig. 17). We retrieve a curve very similar to the variation captured in Fig. 14, demonstrating that the trends in the role of aspect ratio on the yield strength based on the micro Hall-Petch equation can be captured to a good extent using simple theoretical arguments.

While our proposed approach provides one way to incorporate the micro Hall-Petch equation in crystal plasticity, this approach can be refined in multiple ways, a few of which we note below:

1) Presently, the maximum compatibility factor used in the model is solely dependent on the orientation of neighboring grains and the slip systems under consideration. This maximum compatibility factor can further be refined to include the grain boundary inclinations, which formed an important part of our previous work [49,50]. This, however, must also be supplemented with usage of microstructure meshes which can furnish this information of the grain boundary inclinations and that this information is independent of the meshing itself. More importantly, apart from texture and grain size distributions, some information associated with the grain boundary inclinations must also be included in synthetic microstructure generation algorithms. This lack of inclusion of grain boundary inclinations in our current approach makes it particularly easy to interface with existing synthetic microstructure generation software, but at the expense of not including grain boundary geometry information.
2) The micro Hall-Petch coefficients obtained from our previous work involving localized experiments associated with slip bands blocked by grain boundaries, are not in agreement with the parameters obtain post-calibration with stress-strain curves. This is not unexpected since the basis of these two approaches is quite different – pile-up stress measurements are localized while crystal plasticity constitutive modeling is homogenized. One possible line of study could be trying to relate the two sets of coefficients through some multiscale modeling approach, in which the micro Hall-Petch coefficients obtained from calibration can be derived (to some degree of approximation) through coarse graining the micro Hall-Petch coefficients obtained from pile-up stress studies.
3) While the micro Hall-Petch modification was incorporated for basal and prismatic slip systems, extending the approach to twinning is a natural next step. To accomplish this will involve developing a model to obtain expressions of the pile-up stress ahead of a twin blocked by a grain boundary. There has been some earlier work in the description of twins using dislocation models [74–77] and associated applications [78–81]. This work can be integrated with experimental pile-up stress measurements ahead of

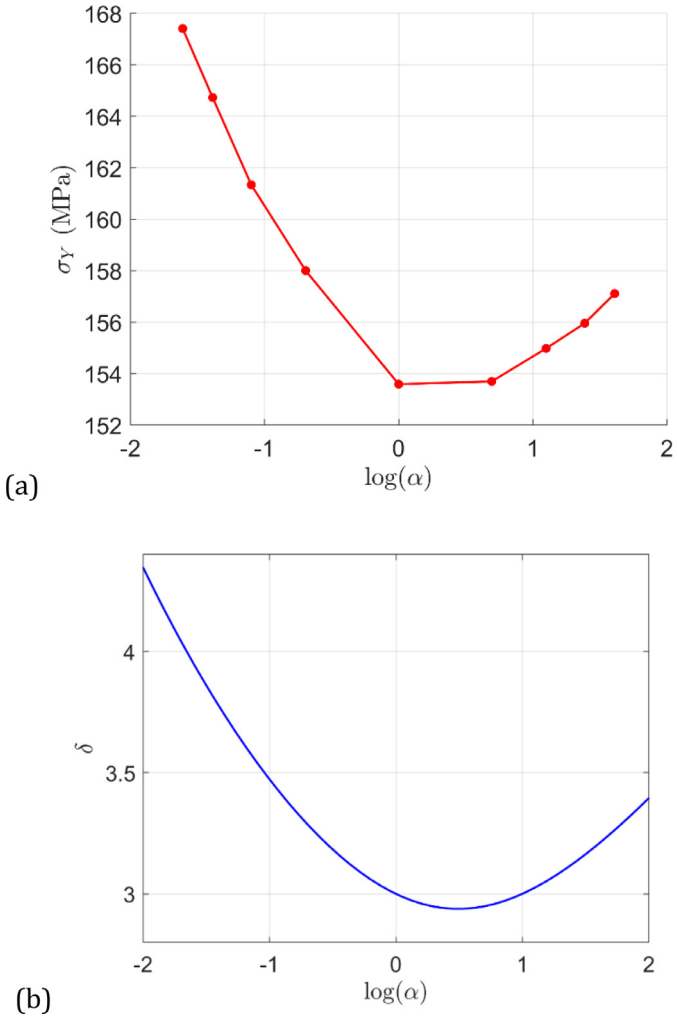

Fig. 17. (a) Variation of yield strength with aspect ratio (b) δ plotted against log (α) as described in Eq. (19).

a twin blocked by a grain boundary and then relate the micro Hall-Petch parameters to some measure of compatibility [82–85].

4. Conclusions

A procedure to incorporate the micro Hall-Petch equation into a CPFE framework to simulate the plastic behavior of microstructures including the grain size and texture effects was developed. We presented a comparison of the stress-strain curves between CPFE and experiments using parameters proposed in previous work, before calibration using four parameters – the basal and prismatic slip resistances and the basal and prismatic micro Hall-Petch multipliers. Using the calibrated parameters, two sets of parametric studies were performed to investigate the Hall-Petch slope predictions - (i) Basal texture superposed with different degrees of spread, and (ii) Angle of loading direction relative to basal poles for strong basal texture. In the first study, the simulations predicted a gradual increase in the Hall-Petch slope with an increase in the spread from $\varepsilon = 5$ to $\varepsilon = 15$, which then increased drastically towards $\varepsilon = 30$. The reduction in maximum compatibility factor with delocalization of texture combined with increasing basal slip contribution dominates the effect of reduced twinning activity, resulting in a gradual increase in the Hall-Petch slope. The subsequent increase in Hall-Petch slope was attributed to an increase in prismatic slip activity combined with further texture delocalization, where the high micro Hall-Petch coefficient for prismatic systems contributes to this increase. In the second study, the simulations predicted a decrease in the Hall-Petch slope with the angle of loading direction from $\varphi = 0^o$ to $\varphi = 45^o$ which was explained based on the domination of a decrease in twinning activity compared to an increase in the basal activity where the localized basal texture reduced the contribution of basal slip due to maximum compatibility factors close to one. The increase in Hall-Petch slope from $\varphi = 45^o$ to $\varphi = 90^o$ was attributed to the high micro Hall-Petch coefficient for prismatic slip combined with the increase in prismatic activity, against the decrease in basal activity. Finally, the effect of the aspect ratio on the yield strength of as-extruded microstructures was studied to obtain a non-monotonic dependence of the yield strength on the logarithm of the aspect ratio. This qualitative trend was derived using the inverse square-root dependence of the yield strength on a measure of the slip system-level grain size, combined with simple geometry, crystallography, and basic plasticity assumptions. Through this we demonstrate a theoretical approach to explain the effect of texture and the grain morphology on the yield strength and plastic stress-strain response.

Our proposed approach to incorporate the micro Hall-Petch equation into crystal plasticity provides a foundation to quantitatively model more complicated scenarios of coupling between grain size, texture and loading direction in the plasticity of Mg alloys. When combined with our previous work on this topic, it provides an integrated framework of combining theory, experiment, and computation to build models incorporating the grain size effect in plasticity for arbitrary alloy systems.

Code availability

PRISMS-Plasticity is an open-source software available for download at https://github.com/prisms-center/plasticity. In addition to written tutorials available in the GitHub repositories, a series of video tutorials totaling nearly two and three hours of content are available at https://www.youtube.com/playlist?list=PL4yBCojM4Swqy4FRteqxHWSiM1uiOOesj . The MATLAB script to compute the micro Hall-Petch parameters for microstructural points given the microstructural information as input, is available at https://github.com/prisms-center/prisms-toolbox/tree/master/PRISMS-Plasticity-Toolbox/Micro_Hall_Petch .

Data availability

All the CPFE input files, microstructures, PRISMS-CPFE simulation results and experimental datasets are available on Materials Commons at https://doi.org/10.13011/m3-a93n-y666.

Declaration of Competing Interest

The authors declare that they have no known competing financial interests or personal relationships that could have appeared to influence the work reported in this paper.

Acknowledgments

This work was supported by the U.S. Department of Energy, Office of Basic Energy Sciences, Division of Materials Sciences and Engineering under Award #DE-SC0008637 as part of the Center for PRedictive Integrated Materials Science (PRISMS Center) at the University of Michigan. We acknowledge with appreciation the assistance of Bruce Williams of CANMET Materials who provided the materials used in this study. Electron microscopy studies were conducted at the Michigan Center for Materials Characterization at the University of Michigan. This work used the Extreme Science and Engineering Discovery Environment (XSEDE), which is supported by National Science Foundation grant number ACI-1548562, through the allocation TG-MSS160003.

References

[1] H. Furuya, N. Kogiso, S. Matunaga, K. Senda, Mater. Sci. Forum, Trans. Tech. Publ. (2000) 341–348.
[2] M. Easton, M. Gibson, A. Beer, M. Barnett, C. Davies, Y. Durandet, S. Blacket, X. Chen, N. Birbilis, T. Abbott, Sustainable Automot. Technol. (2012) 17–23 Springer2012.
[3] U. Riaz, I. Shabib, W. Haider, J. Biomed. Mater. Res. Part B: Appl. Biomater. 107 (6) (2019) 1970–1996.
[4] N. Stanford, J. Geng, Y.B. Chun, C.H.J. Davies, J.F. Nie, M.R. Barnett, Acta Mater. 60 (1) (2012) 218–228.
[5] J.-F. Nie, Metall. Mater. Trans. A 43 (11) (2012) 3891–3939.

[6] J.D. Robson, N. Stanford, M.R. Barnett, Acta Mater. 59 (5) (2011) 1945–1956.
[7] X. Ma, Q. Jiao, L.J. Kecskes, J.A. El-Awady, T.P. Weihs, Acta Mater. 189 (2020) 35–46.
[8] A. Singh, M. Nakamura, M. Watanabe, A. Kato, A. Tsai, Scr. Mater. 49 (5) (2003) 417–422.
[9] B. Wu, Y. Zhao, X. Du, Y. Zhang, F. Wagner, C. Esling, Mater. Sci. Eng.: A 527 (16–17) (2010) 4334–4340.
[10] S. Sandlöbes, Z. Pei, M. Friák, L.-F. Zhu, F. Wang, S. Zaefferer, D. Raabe, J. Neugebauer, Acta Mater. 70 (2014) 92–104.
[11] Q. Yang, A. Ghosh, Acta Mater. 54 (19) (2006) 5159–5170.
[12] B. Guan, Y. Xin, X. Huang, P. Wu, Q. Liu, Acta Mater. 173 (2019) 142–152.
[13] W. Yuan, S. Panigrahi, J.-Q. Su, R. Mishra, Scr. Mater. 65 (11) (2011) 994–997.
[14] H. Yu, Y. Xin, M. Wang, Q. Liu, J. Mater. Sci. Technol. 34 (2) (2018) 248–256.
[15] E. Hall, Proc. Phys. Soc. London Sect. B 64 (9) (1951) 747.
[16] N. Petch, J. Iron Steel inst. 174 (1953) 25–28.
[17] J. Eshelby, F. Frank, F. Nabarro, Lond., Edinburgh, Dublin Philos. Mag. J. Sci. 42 (327) (1951) 351–364.
[18] R. Armstrong, Metall. Mater. Trans. B 1 (5) (1970) 1169–1176.
[19] S. Razavi, D. Foley, I. Karaman, K. Hartwig, O. Duygulu, L. Kecskes, S. Mathaudhu, V. Hammond, Scr. Mater. 67 (5) (2012) 439–442.
[20] Y. Wang, C. Chang, C. Lee, H. Lin, J. Huang, Scr. Mater. 55 (7) (2006) 637–640.
[21] L.L. Shaw, A.L. Ortiz, J.C. Villegas, Scr. Mater. 58 (11) (2008) 951–954.
[22] L. Guo, Z. Chen, L. Gao, Mater.Sci. Eng.: A 528 (29–30) (2011) 8537–8545.
[23] L. Tong, M. Zheng, S. Kamado, D. Zhang, J. Meng, L. Cheng, H. Zhang, J. Magn. Alloys 3 (4) (2015) 302–308.
[24] Y. Wang, H. Choo, Acta Mater. 81 (2014) 83–97.
[25] Y. Wen, B. Guan, Y. Xin, C. Liu, P. Wu, G. Huang, Q. Liu, Scr. Mater. 210 (2022) 114451.
[26] Z.C. Cordero, B.E. Knight, C.A. Schuh, Int. Mater. Rev. 61 (8) (2016) 495–512.
[27] H. Yu, C. Li, Y. Xin, A. Chapuis, X. Huang, Q. Liu, Acta Mater. 128 (2017) 313–326.
[28] R. Hill, J. Mech. Phys. Solids 14 (2) (1966) 95–102.
[29] R. Hill, J. Rice, J. Mech. Phys. Solids 20 (6) (1972) 401–413.
[30] R.J. Asaro, J. Rice, J. Mech. Phys. Solids 25 (5) (1977) 309–338.
[31] R. Hill, K. Havner, J. Mech. Phys. Solids 30 (1–2) (1982) 5–22.
[32] D. Peirce, R. Asaro, A. Needleman, Acta Metall. 30 (6) (1982) 1087–1119.
[33] M. Yaghoobi, G.Z. Voyiadjis, V. Sundararaghavan, cryst. 11 (4) (2021) 435.
[34] H. Gao, Y. Huang, W. Nix, J. Hutchinson, J. Mech. Phys. Solids 47 (6) (1999) 1239–1263.
[35] N. Fleck, G. Muller, M.F. Ashby, J.W. Hutchinson, Acta Metall. Mater. 42 (2) (1994) 475–487.
[36] A. Acharya, J. Bassani, A. Beaudoin, Scr. Mater. 48 (2) (2003) 167–172.
[37] P. Gudmundson, J. Mech. Phys. Solids 52 (6) (2004) 1379–1406.
[38] G.Z. Voyiadjis, M. Yaghoobi, Size Effects In Plasticity: From Macro to Nano, Academic Press, 2019.
[39] A. Lakshmanan, M. Yaghoobi, K.S. Stopka, V. Sundararaghavan, J. Mater. Res. Technol. 19 (2022) 3337–3354.
[40] A. Jain, S. Agnew, Mater. Sci. Eng.: A 462 (1–2) (2007) 29–36.
[41] A. Jain, O. Duygulu, D. Brown, C. Tomé, S. Agnew, Mater. Sci. Eng.: A 486 (1–2) (2008) 545–555.
[42] B. Raeisinia, S.R. Agnew, A. Akhtar, Metall. Mater. Trans. A 42 (5) (2011) 1418–1430.
[43] M.A. Kumar, I.J. Beyerlein, C.N. Tome, J. Appl. Phys. 120 (15) (2016) 155105.
[44] M.A. Kumar, I.J. Beyerlein, Mater. Sci. Eng.: A 771 (2020) 138644.
[45] I. Beyerlein, R. McCabe, C. Tomé, J. Mech. Phys. Solids 59 (5) (2011) 988–1003.
[46] S. Ganesan, M. Yaghoobi, A. Githens, Z. Chen, S. Daly, J.E. Allison, V. Sundararaghavan, Int. J. Plast. 137 (2021) 102917.
[47] B. Ravaji, S.P. Joshi, Acta Mater. 208 (2021) 116743.
[48] M. Taheri Andani, A. Lakshmanan, M. Karamooz-Ravari, V. Sundararaghavan, J. Allison, A. Misra, Sci. Rep. 10 (1) (2020) 1–8.
[49] M. Taheri Andani, A. Lakshmanan, V. Sundararaghavan, J. Allison, A. Misra, Acta Mater. 200 (2020) 148–161.
[50] M. Taheri Andani, A. Lakshmanan, V. Sundararaghavan, J. Allison, A. Misra, Acta Mater. 226 (2022) 117613.
[51] J. Luster, M. Morris, Metall. Mater. Trans. A 26 (7) (1995) 1745–1756.
[52] E. Bayerschen, A. McBride, B. Reddy, T. Böhlke, J. Mater. Sci. 51 (5) (2016) 2243–2258.
[53] M. Yaghoobi, S. Ganesan, S. Sundar, A. Lakshmanan, S. Rudraraju, J.E. Allison, V. Sundararaghavan, Comput. Mater. Sci. 169 (2019) 109078.
[54] M. Yaghoobi, K.S. Stopka, A. Lakshmanan, V. Sundararaghavan, J.E. Allison, D.L. McDowell, npj Comput. Mater. 7 (1) (2021) 1–12.
[55] M. Yaghoobi, Z. Chen, V. Sundararaghavan, S. Daly, J.E. Allison, Integr. Mater. Manuf. Innov. 10 (3) (2021) 488–507.
[56] M. Yaghoobi, Z. Chen, A.D. Murphy-Leonard, V. Sundararaghavan, S. Daly, J.E. Allison, Int. J. Plast. (2022) 103345.
[57] M. Yaghoobi, J.E. Allison, V. Sundararaghavan, Integr. Mater. Manuf. Innov. (2022) 1–18.
[58] E. Kröner, Arch. Ration. Mech. Anal. 4 (1) (1959) 273–334.
[59] E.H. Lee, Elastic-Plastic Deformation at Finite Strains, 1969.
[60] R.J. Asaro, A. Needleman, Acta Metall. 33 (6) (1985) 923–953.
[61] L. Anand, Int. J. Plast. 1 (3) (1985) 213–231.
[62] S.R. Kalidindi, C.A. Bronkhorst, L. Anand, J. Mech. Phys. Solids 40 (3) (1992) 537–569.
[63] C.N. Tomé, R.A. Lebensohn, U.F. Kocks, Acta Metall. Mater. 39 (11) (1991) 2667–2680.
[64] D. Arndt, W. Bangerth, B. Blais, T.C. Clevenger, M. Fehling, A.V. Grayver, T. Heister, L. Heltai, M. Kronbichler, M. Maier, J. Numer. Math. 28 (3) (2020) 131–146.
[65] E. Nieto-Valeiras, S. Haouala, J. LLorca, Eur. J. Mech. A. Solids 91 (2022) 104427.
[66] M.A. Groeber, M.A. Jackson, Integr. Mater. Manuf. Innov. 3 (1) (2014) 56–72.
[67] R. Hielscher, H. Schaeben, J. Appl. Crystallogr. 41 (6) (2008) 1024–1037.
[68] H. Schwartz, Metals Alloys 5 (1934) 139.
[69] E. Scheil, A. Lange-Weise, Verlag Stahleisen (1935).
[70] S. Saltykov, Plant Lab. 15 (11) (1949) 1317–1319.
[71] L.J. Slutsky, C. Garland, Phys. Rev. 107 (4) (1957) 972.
[72] T. Long, C.S. Smith, Acta Metall. 5 (4) (1957) 200–207.
[73] A. Akhtar, E. Teghtsoonian, Philos. Mag. 25 (4) (1972) 897–916.
[74] R. Cahn, Nuovo Cimento 10 (4) (1953) 350–386 1943-1954.
[75] B.A. Bilby, A. Crocker, Proc. R. Soc. Lond. Ser. A. Math. Phys. Sci. 288 (1413) (1965) 240–255.
[76] A. Seeger, Acta Crystallogr. 20 (2) (1966) 323 -323.
[77] A.d.M. Kosevich, V. Boĭko, Soviet Phys. Uspekhi 14 (3) (1971) 286.
[78] M.H. Yoo, C.-T. Wei, Philos. Mag. 13 (124) (1966) 759–775.
[79] T. Mitchell, J. Hirth, Acta Metall. Mater. 39 (7) (1991) 1711–1717.
[80] S. Kamat, J. Hirth, P. Müllner, Philos. Mag. A 73 (3) (1996) 669–680.
[81] J. Lloyd, Proc. R. Soc. A: Math., Phys. Eng. Sci. 474 (2210) (2018) 20170709.
[82] L. Wang, Y. Yang, P. Eisenlohr, T. Bieler, M. Crimp, D. Mason, Metall. Mater. Trans. A 41 (2) (2010) 421–430.
[83] M.A. Kumar, I.J. Beyerlein, R.J. McCabe, C.N. Tome, Nat. Commun. 7 (1) (2016) 1–9.
[84] M.A. Kumar, I. Beyerlein, R. Lebensohn, C. Tomé, Modell. Simul. Mater. Sci. Eng. 25 (6) (2017) 064007.
[85] J. Kacher, J.E. Sabisch, A.M. Minor, Acta Mater. 173 (2019) 44–51.

Please cite this article as: A. Lakshmanan, M.T. Andani, M. Yaghoobi et al., A combined experimental and crystal plasticity study of grain size effects in magnesium alloys, Journal of Magnesium and Alloys, https://doi.org/10.1016/j.jma.2023.05.008